AGU PUBLICATIONS

Tectonics

RESEARCH ARTICLE
10.1002/2017TC004619

Special Section:
Orogenic cycles: from field observations to global geodynamics

Thermochronometry Across the Austroalpine-Pennine Boundary, Central Alps, Switzerland: Orogen-Perpendicular Normal Fault Slip on a Major "Overthrust" and Its Implications for Orogenesis

Jason B. Price[1], Brian P. Wernicke[1], Michael A. Cosca[2], and Kenneth A. Farley[1]

[1]Division of Geological and Planetary Sciences, California Institute of Technology, Pasadena, CA, USA, [2]Geology, Geophysics, and Geochemistry Science Center, U.S. Geological Survey Denver, CO, USA

Key Points:
- Thermal histories of the Austroalpine hanging wall and Pennine footwall, constrained by nine thermochronometric systems, show that they did not thermally equilibrate until after 29 Ma, and possibly not until 18 Ma
- The thermal data indicate that the Austroalpine-Pennine contact zone is a top-south to top-southeast normal fault with at least 60 km of displacement, active during the main phase of Alpine mountain building
- Development of topography and an orogenic crustal root, as reflected in deposition of the perialpine molasse and deformation of Europe (Helvetics) circa 33-15 Ma, may result primarily by buoyancy-driven interposition of the Pennine zone between the Austroalpine "lid" and the European cratonal margin and not from the convergence between Apulia and Europe

Supporting Information:
- Supporting Information S1
- Figure S1
- Figure S2
- Figure S3
- Table S1
- Table S2
- Table S3
- Table S4
- Table S5

Correspondence to:
J. B. Price,
jboprice@gmail.com

Citation:
Price, J. B., Wernicke, B. P., Cosca, M. A., & Farley, K. A. (2018). Thermochronometry across the Austroalpine-Pennine boundary, Central Alps, Switzerland: Orogen-perpendicular normal fault slip on a major "overthrust" and its implications for orogenesis. *Tectonics*, *37*, 724–757. https://doi.org/10.1002/2017TC004619

Received 14 APR 2017
Accepted 14 NOV 2017
Accepted article online 13 DEC 2017
Published online 7 MAR 2018

Abstract Fifty-one new and 309 published thermochronometric ages (nine systems with closure temperatures ranging from ~450 to 70°C) from the Graubünden region of the Central Alps demonstrate that a pronounced thermal mismatch between the Austroalpine allochthon (Alpine "orogenic lid") and the Pennine zone persisted until at least 29 Ma and, allowably, until circa 18 Ma. The observed mismatch supports previous suggestions that the famous "overthrust" between the Austroalpine allochthon and the Pennine zone, historically regarded as primarily an Eocene top-north thrust fault, is in fact primarily an Oligocene-Miocene normal fault that has a minimum of 60 km of displacement with top-south or top-southeast sense of shear. Two hallmarks of Alpine geology, deposition of the foredeep Molasse and emplacement of the Helvetic nappes, appear to be coeval, peripheral manifestations of crustal thickening via the interposition of the Pennine zone as a northward intruding wedge between the Austroalpine "lid" and the European cratonic margin, with the Helvetic system (European margin) acting as the "floor" of the wedge. We presume the Penninic wedge is driven by the buoyant rise of subducted crust no longer able to remain attached to the descending slab. If so, emplacement of the Pennine wedge could have occurred mainly after Adria was juxtaposed against cratonic Europe.

Plain Language Summary What causes mountains to rise? The most common setting for their development is a place where the Earth's tectonic plates collide. Like the jaws of a closing vice, the plates squeeze crust between them, greatly deforming it by faulting and folding. One of the best known examples of this complex process is the European Alps, which formed between colliding continental plates of Europe and "Adria" (Italy). The traditional view is that large faults within the Alps are a direct expression of the sliding of the southern margin of the European plate beneath Adria (a process called subduction) to great depths in the Earth (100 km or more). Here we analyze the timing of motion of the largest fault in the Alps of eastern Switzerland (the Austroalpine "overthrust") using a variety of thermochronometers (heat-sensitive "clocks" that provide time of cooling). Our results show that the timing and sense of motion on the fault do not reflect relative motion between the two plates as previously believed. Instead, displacement on the faults we now see within the mountain belt mainly occurred late in the collision process, when the mechanical attachment of the subducted European crust to the downgoing plate was lost due to heating, which caused it to buoyantly rise relative to its dense surroundings in the Earth's mantle. Returning this wedge of crust to near the surface greatly thickened the overall crust along the collisional "suture" of the two continents, causing the Alps to rise.

1. Introduction

Since the advent of plate tectonics a half-century ago, there has been widespread agreement that mountain belts in the Alpine-Himalaya system formed as a consequence of convergence between continental plates, as an end-phase of oceanic subduction (e.g., McKenzie, 1972; McKenzie & Sclater, 1971). Consensus was supported by the observation that most of these orogens feature horizontal contraction along their flanks and have thicker crust than their surrounding lowlands. More gradually, it was noted that the cores of these orogens had been affected to varying degrees by horizontal extension and vertical thinning, along presumed fossil subduction channels and within the broader collision zone (e.g., Burchfiel & Royden, 1985; Dewey, 1988; Ernst, 1975, 2005; Lister et al., 1984; Selverstone, 1988). The role such structures play in the

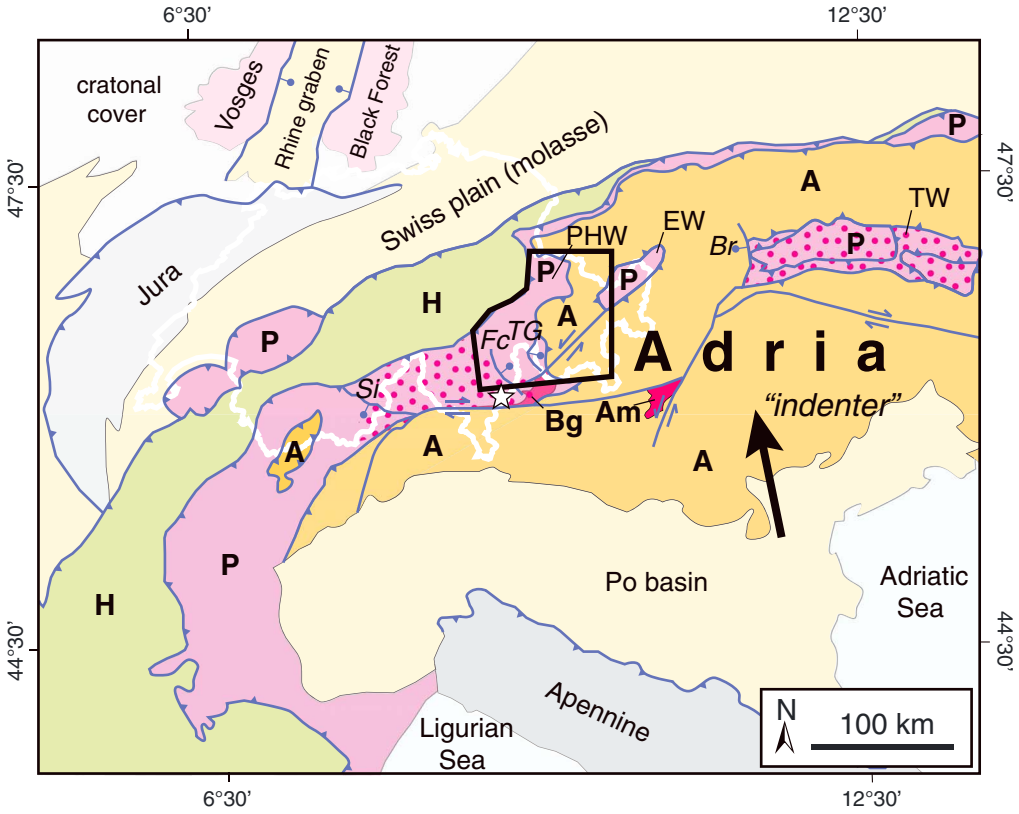

Figure 1. Generalized tectonic map of Switzerland (outlined in white) and environs. The large black box outlines the study area. Large black arrow indicates general movement direction of the modern Adriatic sub-plate (Italy). Thrust faults are shown with teeth on the hanging wall. Several discrete normal faults (ball-and-bar on hanging wall) are mapped: Simplon (Si), Forcola (Fc), Turba mylonite-Gürgaletsch shear zone (TG), and Brenner fault (Br). Tectonic windows shown are Engadine window (EW), Prättigau (aka Northern) half-window (PHW), and Tauern window (TW). Major tectonic elements include Adamello pluton (Am), Austroalpine-South Alpine domain (A), Bergell pluton (Bg), Helvetic nappes (H), and Pennine zone (P). Stippled region indicates late Barrovian metamorphic overprint of the Lepontine and Tauern regions (e.g., Engi et al., 2004). White star indicates location of UHP eclogite at Monte Duria. Modified after Pfiffner (2010).

development of mountain belts, however, remains controversial, in large measure because of uncertainties in the timing of extensional structures in relation to plate convergence, crustal thickening, and contractile structures. In the case of the Alps, for example, extensional structures have been attributed to synconvergent thinning in the upper crust as it thickens below (e.g., Platt, 1986), episodes of plate divergence during the collision process (e.g., Beltrando et al., 2010; Malusà et al., 2011), midcrustal, orogen-parallel spreading of an accretionary nappe stack (Schmid et al., 2004, 1996), buoyant rise of subducted crust within a subduction channel (e.g., Boutelier et al., 2004; Butler et al., 2013, 2014; Chemenda et al., 1995), and late-collisional or postcollisional modification of the newly thickened crust, including orogen-parallel extension (e.g., Mancktelow, 1992; Selverstone, 2005). In this paper, we explore this problem by focusing on the timing of development of the complex tectonic contact zone between the "metamophic core" of the Alps (Pennine zone), a presumed fossil subduction channel of Eocene age, and the overlying "orogenic lid" (Austroalpine allochthon) where it is most extensively exposed in eastern Switzerland, traditionally referred to as the main Austroalpine overthrust. Our goal is to use thermochronometric analysis to better understand the nature and timing of this juxtaposition, and its relationship to the development of flanking belts of horizontal contraction (e.g., Helvetic nappes), thickened crust, and high topography.

Within subduction channels, the thermal inversion reequilibrates after subduction ceases, causing both footwall and hanging wall to rise in temperature on timescales of order 10 Myr (e.g., Peacock, 1989). In continent-continent collisions, the subduction channel may be either extensionally or erosionally unroofed, either during continued subduction, or afterward. Postkinematic unroofing histories may be rapid or

shallow enough to quench and preserve late-kinematic thermal structure within the upper continental crust, or slow or deep enough such that the late-kinematic thermal structure is overprinted by a conventional geotherm during cooling (e.g., Butler et al., 2013). For example, the Pennine zone (Figure 1) is widely regarded as a fossil, mid-Tertiary subduction channel complex that formed between the colliding Adriatic microplate and the European continent, and includes components ranging in metamorphic grade from subgreenschist to amphibolite and (U)HP eclogite facies (e.g., Angiboust et al., 2011, 2014; Beaumont et al., 2009; Chopin, 2003; Malusà et al., 2011; Wheeler et al., 2001). In the Central Alps, most of the complex is overprinted by a postkinematic Barrovian-type metamorphism (e.g., Burg & Gerya, 2005), followed by relatively steady state unroofing with a stable upper crustal thermal structure (Bernet et al., 2009; Vernon et al., 2008). Throughout most of the complex, low-temperature (50–300°C closure temperature (Tc)) thermochronologic transects show little relationship to structural elements of the subduction channel. Instead, for any given thermochronometer, there is a small positive correlation of age with elevation owing to rapid Neogene erosional unroofing, with most systems yielding Miocene or younger cooling ages (0–20 Ma).

In eastern Switzerland, the boundary between the Austroalpine and Pennine paleogeographic realms (main Austroalpine overthrust and associated structures) is regarded by most workers to be the top of a subduction channel which was active during mid-Tertiary continent-continent collision. Unlike the general pattern of postsubduction thermal reequilibration observed in the Central Alps, however, marked contrasts in early- to mid-Tertiary thermal histories are recorded at different structural levels, and in at least one case, such a contrast has been reported to occur within $\leq$1 km of an important mylonitic shear zone associated with the top of the subduction channel (Augenstein, 2012). A similar pattern is apparent in the Tauern Window region of the Eastern Alps where Penninic and deeper structural levels with late Oligocene and Miocene cooling histories that begin above 300°C are juxtaposed beneath the Austroalpine allochthon, most of which resided at temperatures $<$200°C since the Late Cretaceous to early Tertiary (Luth & Willingshofer, 2008).

Here we report time-temperature histories from sample transects spanning the Pennine-Austroalpine boundary zone in the Central Alps of eastern Switzerland (Figure 1) to help resolve the long-standing problem of the precise age and origin of Pennine nappe structure and its juxtaposition with Austroalpine units. Placing firm limits on the timing of Pennine deformation is frustratingly elusive. The maximum age is usually based on paleontological constraints from metamorphosed, poorly fossiliferous flysch deposits that may predate deformation by tens of millions of years. The minimum age is usually unconstrained by field relationships, because the Alpine orogen is virtually devoid of any pre-Quaternary sedimentary or igneous rocks that cross-cut the nappe structure. The principal existing constraints on the age of Pennine nappe movement in this area are the preservation of Lower Eocene nummulites (less than circa 56 Ma) in predeformational sedimentary rocks (Nänny, 1948; Ziegler, 1956) and the truncation of some of the nappe boundaries and associated fabric by the circa 30 Ma Bergell pluton (Hansmann, 1996). The best hope for improving these constraints lies in identifying and dating metamorphic and/or synkinematic mineral phases that grew near or below their closure temperatures (i.e., Alpine-stage titanite at Dora Maira massif, Rubatto & Hermann, 2001; Alpine-stage zircon overgrowths at Monte Duria, Adula nappe, Hermann et al., 2006), or, outside of that, using a series of thermochronometers to document abrupt discontinuities in thermal history across nappe boundaries, which may yield a maximum age for the cessation of their movement (e.g., Augenstein, 2012; Campani et al., 2010; Inger et al., 1996; Malusà et al., 2005). In addition, thermal history also has the potential to constrain the minimum offsets along major structures as it often does in extensional terrains, such as the Basin and Range province of western North America (Fitzgerald et al., 2009, 1991; Reiners et al., 2000; Stöckli, 2005).

For problems of tectonic deformation in the low-temperature regime of subduction channels, the ideal thermochronometric tools are zircon fission track (ZFT; nominal Tc of ~240°C) and zircon (U-Th)/He (ZHe; nominal Tc of ~180°C) dating. In the Pennine zone of eastern Switzerland, the high-pressure, hydrous inosilicate carpholite ($P >$ ~1 GPa) is common in even the lowest-temperature portions of the complex (e.g., Wyss & Isler, 2011). However, peak metamorphic temperatures are generally subgreenschist facies ($<$400°C, e.g., Figure 15 in Mählmann, 2001; Miron et al., 2013; Schreurs, 1993; Wyss & Isler, 2011), occurring within 200°C of ZFT and ZHe closure temperatures. In most thermomechanical models (e.g., Figure 4 in Gerya, Stöckhert, & Perchuk, 2002; Figure 4b in Butler et al., 2013), the temperature range 200–450°C spans the active subduction channel from depths ranging from circa 10 to 90 km (0.3 to 3 GPa), at plate convergence rates and time scales appropriate to Alpine collision zone (circa 1–3 cm/yr and 10 to 30 Myr, respectively; Figure 2a). Thus, with a Tc of 350–450°C, Ar/Ar systematics in white mica are well suited to capture the timing of peak metamorphism,

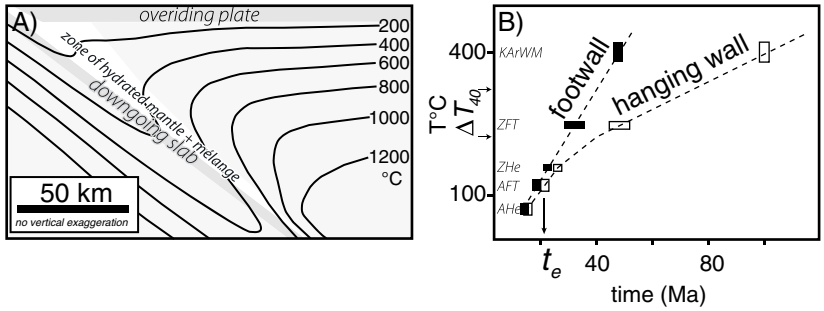

Figure 2. (a) Stretched isotherms in a subduction zone indicate a very shallow thermal gradient of ~8°C/km. As a result, depths (and lithostatic pressures) a factor of four or five greater can be obtained compared to the average continental geotherm of 25–30°C/km (modified after Gerya et al., 2002). (b) Schematic temperature-time cooling paths of two rock masses with different cooling histories: quick cooling (solid boxes) at a rate of ~10°C/Myr versus slow cooling (open boxes) at a rate of 3–4°C/Myr. ΔT_{40} is the difference in temperature between the two rock masses at 40 Ma, and t_e is the approximate time at which thermal equilibrium is attained. Note that because of varying thicknesses of the rock masses, differences in internal radioactive heating, and other extrinsic properties, the two rock masses, while conjoined, never achieve the exact same temperature.

including the possibility of sub-Tc grain growth (Hunziker, 1986; Hunziker et al., 1986; Schreurs, 1993). However, the Ar/Ar system in micas is generally poorly suited to record what is likely to be a protracted history of cooling and tectonism in the late stages of subduction channel evolution (Beaumont et al., 2009; Butler et al., 2013, 2014; Gerya et al., 2002). At temperatures near and below ZFT and ZHe closure, subduction channel isotherms become strongly influenced by proximity to the thermal boundary condition at the Earth's surface. For this reason, apatite thermochronometers (fission track, nominal Tc ~110°C and (U-Th)/He, nominal Tc ~70°C) tend to record processes related primarily to postkinematic erosion and landform evolution (e.g., Bernet et al., 2001, 2009; House, Wernicke, & Farley, 1998). On the basis of these considerations, multisystem time-temperature cooling paths are expected to show mid-Tertiary cooling from above 400°C to less than 100°C in the footwall. In contrast, cooling through a similar temperature range in the hanging wall generally began in the Mesozoic and ended at some point in mid-Tertiary time, near the time that subduction channel activity ceased. By measuring mica, zircon, and apatite cooling ages in both hanging wall and footwall, the two cooling curves define two parameters of interest. The first is the difference in temperature between the hanging wall and footwall cooling paths, hereafter referred to as ΔT, near peak metamorphic temperatures (Figure 2b). The second is the time at which the two paths merge, indicating thermal equilibrium between hanging wall and footwall, hereafter referred to as t_e.

2. Geologic Setting and Previous Work

The primary post-Hercynian, pre-Alpine paleogeographic elements of the Central Alps include, from north to south (Figure 1), the former European continental margin (Helvetic and Ultrahelvetic domains); the tripartite Pennine zone (Valaisan marine trough, Briançonnais rise or "continental ribbon," and Piemont-Ligurian Ocean); and the Adriatic microplate of north African affinity (Austroalpine and South Alpine domains). From Early Jurassic through early Eocene time, Penninic strata were concordantly deposited in marine settings of variable depths that lay between Adria and the European continent. Within Adria, tectonism began in Jurassic time with the development of a highly extended, yet magma-poor, passive margin (Beltrando et al., 2010; Mohn et al., 2010), and continued into the Cretaceous during which time there was an EoAlpine ("Trupchun phase") metamorphic and nappe-stacking event that established the major tectonostratigraphic components of the Austroalpine allochthon (Froitzheim, Schmid, & Conti, 1994; Mohn et al., 2011; Schmid et al., 2004). By the end of the Cretaceous, all but the lowermost elements of the Austroalpine realm had stabilized into a coherent, relatively undeforming unit, at times referred to as a "traineau écraseur" (Argand, 1916) or the "orogenic lid" (Laubscher, 1983). Subduction initiated within the Piemont Ocean during the Late Cretaceous, and by Paleogene time, Briançonnais and Valaisan elements were being subducted under and/or accreted to Adria. The Adriatic microplate began to override the European passive margin (Helvetic domain) during the Eocene (e.g., Schmid et al., 1996). The Cretaceous-Tertiary relative motions between the three domains have long been debated, but to first order, the assembly of the Western and

Central Alps reflects the progressive accretion of elements of the Pennine zone to Adria along one (e.g., Schmid et al., 1996) or multiple (e.g., Froitzheim et al., 2006, 2008) approximately south-dipping subduction zone(s). The structural boundary between the Austroalpine and Pennine domains is preserved in an impressive fault system that can be traced continuously for >400 km along strike of the Alps. The preserved north-south structural overlap between Austroalpine and Penninic units is nearly 150 km in eastern Switzerland and western Austria (e.g., Trümpy, 1960; Schmid et al., 1996, 2004; Figure 1), and the complete mismatch between hanging wall and footwall units along the entire strike length of the fault indicates that this is a minimum amount of displacement.

Normal faulting and extension have long been understood to be integral to the evolution of the Alps, owing to the occurrence of footwall rocks of higher metamorphic grade adjacent to hanging wall rocks (e.g., Platt, 1986), and studies of the *P-T-t* evolution and sense-of-shear along normal fault zones, for example, the Simplon fault (Mancktelow, 1992), Brenner fault (Axen et al., 1995; Selverstone, 1988), Combin Zone (Wust & Silverberg, 1989), and Turba mylonite zone (Nievergelt et al., 1996). These extensional events occurred within a context of cyclic shortening and extension in both Cretaceous and Tertiary time (e.g., Ciancaleoni & Marquer, 2008; Froitzheim et al., 1994, 1996; Handy et al., 1996; Mohn et al., 2011; Nievergelt et al., 1996; Weh & Froitzheim, 2001) and multiple burial and unroofing events of (U)HP metamorphic assemblages in the Pennine zone (e.g., Beltrando et al., 2010; Meyre et al., 1999). Since mid-Tertiary collision in the Alps, a series of tectonometamorphic events, perhaps driven by an Adriatic "indenter" (large arrow in Figure 1) and opening of the Pannonian basin (directly east of the Eastern Alps), has substantially modified the system (e.g., Ratschbacher et al., 1991; Scharf et al., 2013; Schmid et al., 1996), including (1) widespread orogen-parallel extension across the core of the Alps; (2) strike-slip faulting, especially along the southern margin of the Alps on the Periadriatic fault system; (3) folding and thrusting to the north in the Jura Mountains; and (4) Barrovian metamorphic overprint of a large fraction of the Pennine zone in southern Switzerland and northernmost Italy (red dotted area in Figure 1). In addition, modern GPS measurements show that the Adriatic microplate no longer functions as a cohesive whole but is breaking into a series of smaller, independent blocks (Oldow et al., 2002).

2.1. Austroalpine Allochthon

In map view, the trace of the base of the Austroalpine allochthon is sinuous, defining two reentrants or "half windows" (Figure 1). On average, the fault zone dips gently eastward. The hanging wall is a composite of pre-Cenozoic tectonic elements, most recently defined as Lower and Upper Austroalpine, according to their interpreted Jurassic paleogeographic position (Mohn et al., 2011). Lower Austroalpine nappes (Err-Bernina and related digitations) are exposed only in the southern half-window. Upper Austroalpine nappes comprise the more northerly portions of the allochthon, north and east of the southern half-window (Figure 3). The Austroalpine nappes generally contain Mesozoic cover sequences nonconformably resting on extensively exposed crystalline substrates. The crystalline rocks comprise voluminous silicic to intermediate orthogneisses which formed during the late Paleozoic Hercynian (Variscan) orogeny. These sequences were dismembered by crustal-scale extensional and strike-slip faulting in the Mesozoic, which established the general architecture of the future Alpine nappes, and created dramatic juxtapositions of disparate crustal and mantle structural levels during the formation of the northwest Adriatic passive margin (Mohn et al., 2011, 2012; Schuster et al., 2001; Schuster & Frank, 1999).

Following passive margin formation, the tectonic assembly of the allochthon occurred in four main phases (D1–D3, plus "post-D3" deformation; Froitzheim et al., 1996; Handy et al., 1996; Mohn et al., 2011). The first and second, of mid-to Late Cretaceous age, include west-directed imbricate thrusting and folding (in several places reactivating older Jurassic normal faults), followed by extension, most profoundly along a shear zone localized near the base of the Austroalpine units ("Lunghin-Mortirolo movement zone" of Mohn et al., 2011). Below this shear zone, the Margna-Sella nappe complex and Malenco ultramafic zone, which formed along the ocean-continent transition northwest of Adria, were metamorphosed at midcrustal pressures and exhumed along the shear zone and juxtaposed with upper crustal levels. In the third phase (D3), the entire Austroalpine allochthon was juxtaposed against its Penninic substrate beginning in Eocene time. Despite the large displacements implied by the complete mismatch of hanging wall and footwall units across the base of the Austroalpine allochthon, deformation within the allochthon was restricted to east trending, shallowly plunging folds. The "post-D3" phase of deformation, localized near the base of the Austroalpine

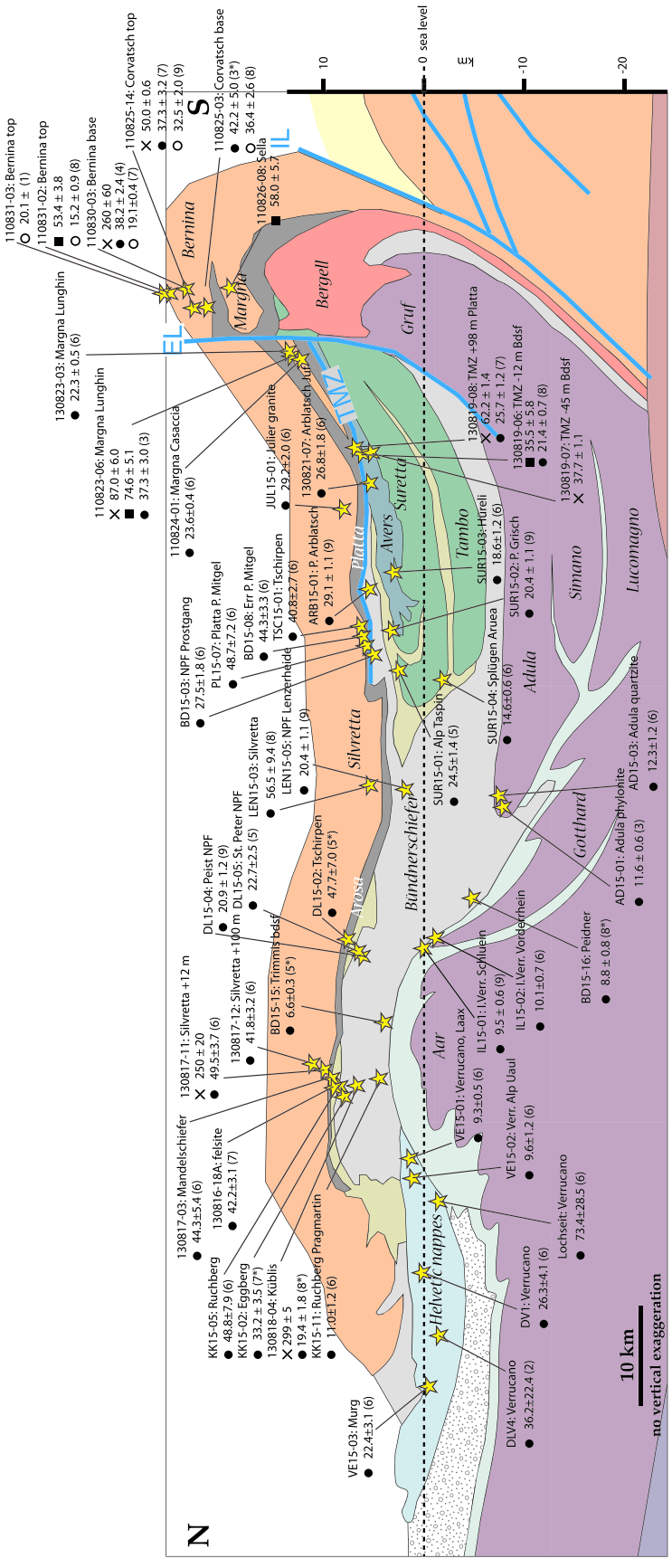

Figure 3. North-south cross section through the Central Alps along easting line 755,000 (1903 Swiss Grid), modified after Schmid et al., 1996, 2004. All cooling ages shown here are new from this study and are a subset of a larger new data set presented in Price (2017). Helvetic and Infrahelvetic ZHe ages shown in the cross section are not discussed in this manuscript. Yellow star indicates sample tectonic position; symbology with cooling ages follows key in Figure 4 (letter-x: white mica $^{40}Ar/^{39}Ar$, filled square: ZFT, filled circle: ZHe, and open circle: AHe).

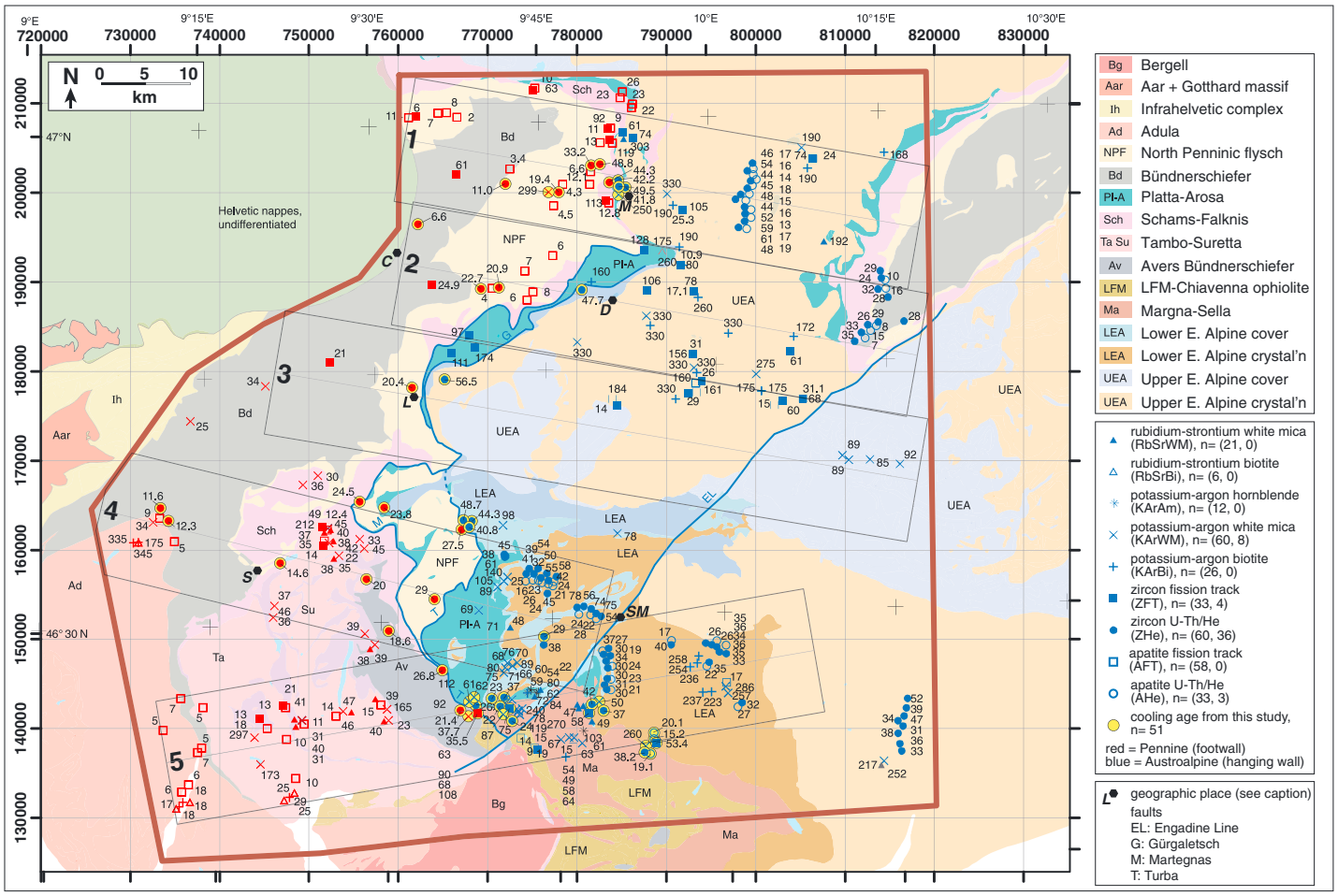

Figure 4. Tectonic map of the study area showing nappes, cooling age samples, and numbered cross sections. Buffers drawn around cross sections project 7 km out from the midline. Ages that fall outside of the buffer are projected to the nearest cross section. All new age dates on the map are archived in the EarthChem data repository (Price et al., 2017). LFM: Lizun-Forno-Malenco. Geographical locations: C, Chur; D, Davos; L, Lenzerheide; M, Madrisahorn; S, Splügen; SM, St. Moritz.

allochthon, resulted in the development of the composite Turba, Gürgaletsch, and Martegnas shear zones (Figures 3 and 4), discussed further below.

2.2. Penninic Substrate of the Austroalpine Allochthon

The structure of the Penninic units in the Central Alps is dominated by a 15–20 km-thick stack of recumbent nappes with amplitudes of up to 50 km (Figure 3; e.g., Milnes & Pfiffner, 1980; Schmid et al., 1996, 2004). The nappes plunge moderately to gently eastward, forming a map-view cross-section through the stack. The nappes are cored by Hercynian basement and have rounded, lobate northern cores and cuspate southern cores. Unlike the hanging wall of the Austroalpine allochthon, only sparing amounts of Mesozoic cover remain depositionally attached to basement. Prior to recumbent folding, the cover sequences of the basement nappes were tectonically sheared off and "replaced" by Mesozoic calcareous schists and sandstones, from both the Valais and Piemont oceans, collectively referred to as "Bündnerschiefer." In places, the ophiolitic substrates of the Bündnerschiefer are tectonically interposed within it. The two highest basement-cored nappes, Tambo and Suretta (green shading in Figure 3), are most proximal to the base of the Austroalpine allochthon, and their cores are generally regarded as having originally formed the basement rocks of the Briançonnais facies belt or "ribbon continent" (e.g., Schmid et al., 1996). In addition to ophiolitic slices, Mesozoic Briançonnais facies cover is preserved as tectonic slices wrapped around the eastern margin of the Suretta nappe (Schams nappes) and along the base of the Austroalpine allochthon (Falknis and Sulzfluh nappes, light green shading in Figure 3). The youngest sediments in the nappe pile and associated cover nappes are lower Eocene turbiditic sandstones and shales known as the Arblatsch flysch in the south

and Prättigau flysch in the north, collectively called "North Penninic flysch." In the northern half-window, Prättigau flysch appears to grade stratigraphically downward into Bündnerschiefer from the Valais Ocean (e.g., Nänny, 1948; Steinmann, 1994; Trümpy, 1980; Weh, 1998). The large mass of tectonically interleaved Prättigau flysch and Bündnerschiefer is known as the Grava "nappe" (Weh, 1998; Weh & Froitzheim, 2001; gray shading in Figure 3 and "Bd" in Figure 4). In contrast, the Arblatsch flysch occurs as isolated, coherent lenses within and beneath the chaotically deformed, ophiolitic Platta nappe, which generally defines the boundary zone between the Austroalpine and Penninic domains. The southern margins of the underlying Tambo and Suretta nappes are truncated by the Bergell and Novate intrusions (red shading in Figure 3 and unit "Bg" in Figure 4), which have a protracted emplacement history from circa 32 to 25 Ma (Hansmann, 1996; Liati et al., 2000; Oberli et al., 2004). These constraints have long suggested that the nappe stack was assembled entirely in Eocene time.

In Oligocene and Miocene time, rocks of the Pennine zone were juxtaposed above the Helvetic domain, coeval with the development of the northern Alpine molasse foredeep basin and with the formation of the Helvetic nappe complex (Figure 1). The postkinematic Barrovian metamorphism, mainly affecting the Lepontine dome region of the Central Alps (e.g., Vance & O'Nions, 1992), affected the southern part of the nappe stack, peaking at circa 18 Ma (Janots et al., 2009; Wiederkehr et al., 2008). Neogene crustal-scale dome-and-basin structure (i.e., Aar and Lepontine culminations, and Wildstrubel and Rawil depressions) overprints the entire system, accompanied by thrust faulting, normal faulting, and strike-slip faulting (e.g., Insubric shear zone, Simplon fault, and Engadine fault zone, respectively; Figures 1, 3, and 4).

2.3. Position of the Base of Austroalpine Allochthon

In the northern half-window, the Pennine-Austroalpine boundary is defined by the chaotically deformed, ophiolitic Arosa zone, which is similar lithologically to the Platta nappe that defines the boundary in the southern half-window. Although derived predominantly from oceanic domains, both Platta and Arosa appear to include tectonically interposed fragments of the Austroalpine allochthon (e.g., Tschirpen gneiss and Triassic dolomite) in its upper few hundred meters. Structural analysis of the contact between the northern part of the Austroalpine allochthon and the Arosa zone records a history of top-west to top-northwest directed shear followed by top-north shear (Ring et al., 1989, 1988). In contrast, detailed structural studies of the Penninic units just beneath the Austroalpine allochthon, one in the northern half-window and the other just north of the southern half-window (Weh & Froitzheim, 2001, and Nievergelt et al., 1996, respectively) both revealed strong extensional deformational episodes within and between Penninic units below the base of the Austroalpine allochthon. These include the development of a 2 to 3 km-thick zone of south-vergent folding that affects most of the upper boundary of the Grava nappe in the northern half-window; top-south to top-southeast normal simple shear along the Gürgaletsch and Martegnas shear zones between the two half-windows; and top-ENE to top-southeast simple shear along and below the Turba mylonite zone in the southern half-window (Nievergelt et al., 1996; Weh, 1998; Price, 2017; Figures 3 and 4). The combined Gürgaletsch-Turba fault zone is localized near the base of the chaotically dismembered Arosa zone to the north and is depicted by Weh and Froitzheim (2001) and Nievergelt et al. (1996) to descend structurally downward to the south, such that the composite Platta and Margna-Sella nappes are in the hanging wall and the Avers Bündnerschiefer is in the footwall. Similar to the upper part of the Grava nappe, top-south shearing affects the upper half of the Suretta nappe, expressed most vividly by the backthrust "fingers" of basement gneisses preserved there (Figures 3 and 4; Niemet-Beverin fold phases of Milnes & Schmutz, 1978; Milnes & Pfiffner, 1980; Schreurs, 1993; Scheiber et al., 2012). Thus, there is abundant evidence for shearing with a strong top-south component affecting the Penninic-Austroalpine boundary along nearly its entire exposed trace from the northern margin of the Bergell intrusion in the southern half-window to the Landquart Valley in the northern half-window, a north-south distance of 70 km. According to structural reconstructions by Weh (1998), the folding of the Grava nappe during top-south deformation and the offset of North Penninic flysch along the Martegnas shear zone (Prättigau flysch in the northern half-window sheared southward as Arblatsch flysch in the southern half-window) suggest 68 km of top-south simple shear along the base of the Austroalpine allochthon (Figure 5.12 in Weh, 1998).

2.4. Previous Thermochronology

A wealth of thermochronologic data from across the Alps has been published over the last five decades, from recognition of metamorphic ages in certain nappes (Jäger, 1962; Oxburgh et al., 1966; Steiger, 1964),

to multisystem age-elevation transects (e.g., Wagner et al., 1977), to detailed apatite fission track (AFT) and apatite (U-Th)/He (AHe) modeling of landform evolution (e.g., Mahéo et al., 2013; Malusà et al., 2005), periodically summarized in compendia (Hunziker et al., 1992; Vernon et al., 2008) and regional interpretive syntheses (e.g., Hurford et al., 1989; Table 1 in Beltrando et al., 2010). Previous studies that focused on lower temperature (70–240°C) thermochronometers indicate that in regions of highest relief in the Penninic and Helvetic Alps, ages generally range from latest Oligocene to Pliocene, with age-elevation profiles that are quite steep (1 to 4 Myr/km) and that differ in mean age by as much as 15 Myr, depending on the chronometer and location. As noted earlier, age-elevation variations, recorded by AFT and AHe systematics, tend not to correspond to specific nappe boundaries or ductile shear zones. For instance, there is very little difference in apatite ages moving northward from the central Lepontine region across the Infrahelvetic complex to the Aar massif, suggesting that these rocks record the postkinematic descent of the 110°C and 70°C isotherms in late Miocene to Pliocene time (Michalski & Soom, 1990; Rahn, 2005; Wagner et al., 1977). The postkinematic character of these low-temperature systems is indeed evident in the fact that a number of studies have shown that post-20 Ma cooling ages are regionally contourable and reflect patterns of broad warping across the entire Alpine orogen (e.g., Bernet et al., 2004, 2009; Fox et al., 2016; Luth & Willingshofer, 2008; Mahéo et al., 2013; Schlunegger & Willett, 1999).

In the Central and Western Alps, an important structure that affects subgreenschist cooling histories is the Simplon low-angle normal fault, a top-southwest shear zone that juxtaposes the upper and lower parts of the Pennine nappe stack in the Valaisan Alps (Campani et al., 2010; Mancktelow, 1992). Age contrasts across the fault are greatest for systems with $Tc \geq 240°C$, with footwall white mica Ar/Ar ages circa 15 Myr younger than hanging wall ages and footwall ZFT ages 5 to 10 Myr younger than hanging wall ages. However, AFT ages across the same boundary show little, if any, contrast (Figure 13 in Campani et al., 2010).

Other fault zones with discordant hanging wall and footwall cooling histories have been identified southwest of the Simplon low-angle normal fault. Orogen-normal AFT and ZFT transects in the Western Alps in the Aosta Valley and environs show 20 Myr age differences associated with the northeast-striking, intra-Penninic Internal Houillière and Briançonnais Front fault zones (Malusà et al., 2005). In a broad region southeast of the Internal Houillière fault, ZFT and AFT ages average circa 32 and 25 Ma, respectively, although there is much scatter in the AFT ages that may reflect age-elevation effects. To the northwest of the fault zone, ZFT and AFT ages average circa 13 and 4 Ma, respectively, with far less scatter in the AFT ages.

In the Eastern Alps in the Tauern Window, even the earliest K/Ar studies revealed dramatic cooling age contrasts between the Austroalpine allochthon and its Penninic substrate. In the hanging wall, K/Ar mica ages average 77 Ma, whereas footwall K/Ar mica ages average 22 Ma (Oxburgh et al., 1966). The cooling age data of Oxburgh et al. (1966) have been augmented by at least 27 subsequent studies (Figure 1 in Luth & Willingshofer, 2008), which collectively indicate that thermal equilibration between the hanging wall and footwall did not occur until after 20 Ma (Figures 4 and 5 in Luth & Willingshofer, 2008).

As noted above, peak metamorphic conditions in the study area (Figures 1 and 4) are generally subgreenschist facies; but much higher grade, upper amphibolite facies, rocks are present just to the west and south (Wiederkehr et al., 2011). In addition, the UHP rocks at Monte Duria occur in the southernmost part of the Adula nappe (Figure 1; just out of view to the south of Figure 4). They yield U/Pb ages of circa 34 to 33 Ma on zircon equilibrated with spinel peridotite, which is presumably the age of maximum burial and metamorphism for the most internal portions of the Adula nappe (Hermann et al., 2006). Within the study area, subgreenschist cooling ages (Ar in mica and ZFT) span a significant range (mostly between 35 and 15 Ma), leaving considerable uncertainty in the timing of final nappe emplacement and especially in the timing of juxtaposition of the Pennine and Austroalpine domains.

Despite the large scatter in cooling ages within the Austroalpine and Pennine domains, and a scarcity of ZFT and ZHe cooling ages near the boundary between them, existing data nonetheless define a marked regional contrast in cooling histories. It is clear that a general westward younging of all ages in the Pennine domain is fairly continuous and is the result of structural doming and rapid erosion of the Lepontine region after 20 Ma (e.g., Bernet et al., 2009; Fox et al., 2016; Schlunegger & Willett, 1999; Wiederkehr et al., 2009). It is less clear, however, whether the contrast in pre-20 Ma ages between the Austroalpine and Pennine domains in the study area is, (1) a continuation of the observed younging pattern, such that progressively older ages to the east simply reflect a higher structural position along the margins of the Neogene dome (Bernet et al., 2001;

Table 1
Summary of Ages Compiled for This Study and Plotted on the Geologic Map in Figure 4

	System	Published data	New data (this study)
1	AHe	33	3
2	AFT	58	0
3	ZHe	60	36
4	ZFT	33	4
5	KArBi	26	0
6	KArWM	60	8
7	KArAm	12	0
8	RbSrBi	6	0
9	RbSrWM	21	0
	Total	310	51

Note. Published data come from Armstrong et al. (1966), Augenstein (2012), Bachmann et al. (2009), Challandes et al. (2003), Ciancaleoni (2005), Evans (2011), Flisch (1986), Handy et al. (1996), Hanson et al. (1966), Hunziker et al. (1992), Knaus (1990), Mählmann (2001), Michalski and Soom (1990), Peters and Stettler (1987), Philipp (1982), Rahn (2005), Schreurs (1993), Steinitz and Jäger (1981), Thöni (1980), Wagner et al. (1977), Weh (1998), and Wiederkehr et al. (2009).

Evans, 2011); or (2) the result of tectonic exhumation of the Pennine zone on faults that are along or near the main Austroalpine overthrust, at some time prior to Neogene doming (e.g., Augenstein, 2012; Beltrando et al., 2010; Nievergelt et al., 1996). Unfortunately, the current en vogue smooth-contouring approach of thermochronometric ages across the orogen (e.g., Bernet et al., 2001, 2004, 2009; Fox et al., 2016) cannot discriminate between the simple doming and exhumation-by-faulting hypotheses.

3. This Study

To help resolve this ambiguity, it is necessary to determine whether hanging wall and footwall cooling histories in samples in the immediate vicinity of the fault zone (1) are essentially the same, as predicted by the simple doming hypothesis, or (2) contrast strongly, as predicted by the tectonic juxtaposition hypothesis. As noted above, if the Pennine zone represents a fossil subduction channel, its thermal history will be best defined by ZFT and ZHe thermochronometry. However, in the published data set, there are remarkably few ages for these mineral systems in the vicinity of the fault zone, making it difficult to resolve whether the cooling histories conform to one or the other of these predictions. Therefore, the goals of this study include (1) creating a database of all published thermochronometric data in the region; (2) collecting and analyzing samples, particularly ZHe and ZFT, that are complimentary to this database; and (3) estimating the vertical structural position of all samples relative to the main Austroalpine fault and other potentially important structures adjacent to it.

3.1. Published Data Compilation

Three hundred nine published age dates from eastern Switzerland, northern Italy, and western Austria were compiled in a database (Tables 1 and 2; sourced from Armstrong et al., 1966; Augenstein, 2012; Bachmann et al., 2009; Challandes et al., 2003; Ciancaleoni, 2005; Evans, 2011; Flisch, 1986; Handy et al., 1996; Hanson et al., 1966; Hunziker et al., 1992; Knaus, 1990; Mählmann, 2001; Michalski & Soom, 1990; Peters & Stettler, 1987; Philipp, 1982; Rahn, 2005; Schreurs, 1993; Steinitz & Jäger, 1981; Thöni, 1980, Wagner et al., 1977; Weh, 1998; Wiederkehr et al., 2009). A total of nine cooling age mineral systems are included: K/Ar amphibole, K/Ar white mica, K/Ar biotite, Rb/Sr white mica, Rb/Sr biotite, zircon and apatite fission track, and zircon and apatite (U-Th)/He. For this study, K/Ar and Ar/Ar cooling ages are considered to be equivalent. The K/Ar-white mica category includes muscovite, phengite, illite, and "white mica." The K/Ar-amphibole category includes hornblende, glaucophane, riebeckite, and richterite. The K/Ar-biotite category includes biotite, biotite-chlorite, and phlogopite but excludes chlorite. Ages were included in the database without filtering for grain size; that is, white mica size fractions of >6 μm, 6–2 μm, and <2 μm were all included; generally, the coarsest size fraction yielded the oldest age. We exclude four ZHe ages from the Evans (2011) data set: One was an outlier young age from the Engadine Valley adjacent to the Engadine fault from a lone rock sample of uncertain origin; three were outlier old ages from the Err nappe on Piz Nair which overlap Ar/Ar white mica ages reported in Handy et al. (1996).

3.2. Sample Collection

Forty-two rock samples were collected along the Austroalpine-Pennine boundary in both the hanging wall and footwall over a strike length of approximately 70 km. All samples were collected by the authors from surface outcrops and roadcuts. Means of access included car, ski lift, gondola, helicopter, hiking trail, glacier traverse, and technical mountaineering routes. From these 42 samples, we report 51 new thermochronometric ages from $^{40}Ar/^{39}Ar$-white mica, zircon fission track, and zircon and apatite (U-Th)/He systems (Tables 1 and 2; Price et al., 2017).

3.3. Determination of Vertical Structural Position

Samples locations were projected onto five vertical WNW-ESE or ENE-WSW cross sections (Figures 4 and 5), which were oriented to be approximately perpendicular to the strike of the Austroalpine-Pennine boundary.

Table 2
New Ages Presented in This Study

Counter	System	Sample	Nappe	Lithology	Structural-*Z*	Age	Err
1	AHe	110830-03	Bernina	Quartz diorite	6.6	19.09	2.32
2	AHe	110831-02	Bernina	Quartz diorite	7.4	15.22	1.84
3	AHe	110831-03	Bernina	Quartz diorite	6.65	20.1	1.01
4	KArWM	110825-14	Corvatsch	S-C mylonite, augen gneiss	4.9	50	0.6
5	KArWM	110830-03	Bernina	Quartz diorite	6.6	260	60
6	KArWM	130817-11	Silvretta	Gneissic granite	0.23	250	20
7	KArWM	130818-04	Prattigau	Gyrenspitz, gray psammite	−2.45	299	5
8	KArWM	130819-07	Avers	Gray metapelite	−0.05	37.7	1.1
9	KArWM	130819-08	Platta	Spilite	0.1	61.9	1.7
10	KArWM	130819-08b	Platta	Spilite	0.1	62.6	1.2
11	KArWM	130823-03	Margna	Augen gneiss	1.26	87	6
12	ZFT	110823-06	Margna	Augen gneiss	1.28	74.55	10.21
13	ZFT	110826-08	Sella	Orthogneiss	4	58.02	11.43
14	ZFT	110831-02	Bernina	Quartz diorite	7.4	53.38	7.53
15	ZFT	130819-06	Avers	Gray metapelite	−0.05	35.5	11.7
16	ZHe	110824-01	Margna	White mica schist	0.55	23.63	0.35
17	ZHe	110825-03	Corvatsch	S-C mylonite	4.2	42.21	10.15
18	ZHe	110825-14	Corvatsch	S-C mylonite, augen gneiss	4.9	37.34	3.21
19	ZHe	110830-03	Bernina	Quartz diorite	6.6	38.18	2.43
20	ZHe	130816-18A	Tschirpen	Felsite	0.22	42.17	3.08
21	ZHe	130817-03	Falknis	"Mandelschiefer" flysch	0.1	44.26	5.39
22	ZHe	130817–11	Silvretta	Gneissic granite	0.23	49.51	3.74
23	ZHe	130817-12	Silvretta	Gneissic granite	0.26	41.82	3.17
24	ZHe	130818-04	Prattigau	Gyrenspitz, gray psammite	−2.45	19.39	1.84
25	ZHe	130819-06	Avers	Phyllite	−0.05	21.36	0.74
26	ZHe	130819-08	Platta	Spilite	0.1	25.69	1.23
27	ZHe	130819-09	Platta	Spilite	0.22	22.79	1.61
28	ZHe	130821-07	Arblatsch	Val Gronda phyllite	−0.78	26.84	1.79
29	ZHe	130823-03	Margna	Augen gneiss	1.27	22.34	0.54
30	ZHe	AD15-01	Adula	White mica schist	−13.58	11.65	0.62
31	ZHe	AD15-03	Adula	White mica schist	−13.7	12.27	1.17
32	ZHe	ARB15-01	Arblatsch	Coarse-grained psammite	−0.2	29.07	1.11
33	ZHe	BD15-03	Arblatsch	Sandstone	−0.55	27.52	1.84
34	ZHe	BD15-07	Bundnerschiefer	Phyllite	−3.3	23.78	1.56
35	ZHe	BD15-08	Err	Metapsammite	0.33	44.31	3.31
36	ZHe	BD15-15	Bundnerschiefer	Metapelite	−5.85	6.57	0.35
37	ZHe	DL15-02	Tschirpen	Greenschist granitoid	0.32	47.72	6.99
38	ZHe	DL15-04	Prattigau	Sandstone	−3.2	20.88	1.17
39	ZHe	DL15-05	Prattigau	Sandstone	−3.48	22.72	2.48
40	ZHe	JUL15-01	Julier	Julier granodiorite	1.9	29.19	1.95
41	ZHe	KK15-02	Prattigau	Eggberg series, gritstone	−1.1	33.19	3.54
42	ZHe	KK15-05	Prattigau	Ruchberg series, gritstone	−0.65	48.77	7.92
43	ZHe	KK15-11	Prattigau	Pfavigrat series, psammite	−3.4	10.95	1.2
44	ZHe	LEN15-03	Silvretta	Augen gneiss	1.1	56.51	9.38
45	ZHe	LEN15-05	Tomul	Ruchberg series, sandstone	−0.65	20.36	1.08
46	ZHe	PL15-07	Platta	Metadiorite	0.05	48.69	7.22
47	ZHe	SUR15-01	Suretta	Quartz eye porphyry	−4.5	24.5	1.36
48	ZHe	SUR15-02	Suretta	Gneissose granitoid	−3.22	20.43	1.14
49	ZHe	SUR15-03	Suretta	Gneissose granitoid	−1.7	18.55	1.17
50	ZHe	SUR15-04	Tambo-Aruea	Orthogneiss	−8.08	14.59	0.58
51	ZHe	TSC15-01	Tschirpen	Greenschist granitoid	0.06	40.82	2.68

Note. ZHe and AHe ages are mean ages of a population of single grain ages. ZFT ages are pooled ages. $^{40}Ar/^{39}Ar$ ages (KArWM) are integrated ages. Errors are standard error of the mean for ZHe and AHe (1σ) and 95% confidence interval for ZFT and $^{40}Ar/^{39}Ar$. Full data tables, including individual grain ages for ZHe and AHe and step-heated 40/39 ratios for Ar/Ar, are available in the supplementary information and from the EarthChem library, DOI: 10.1594/IEDA/100727.

Orientations of cross sections were rotated to account for slight changes in strike of the crystalline sheet. Attitudes of the contact were constrained using a variety of methods, including (1) solving three-point problems in several locations on the west and east sides of the crystalline sheet, (2) exploiting structural windows to determine position within the allochthon, (3) projecting locations of the contact from

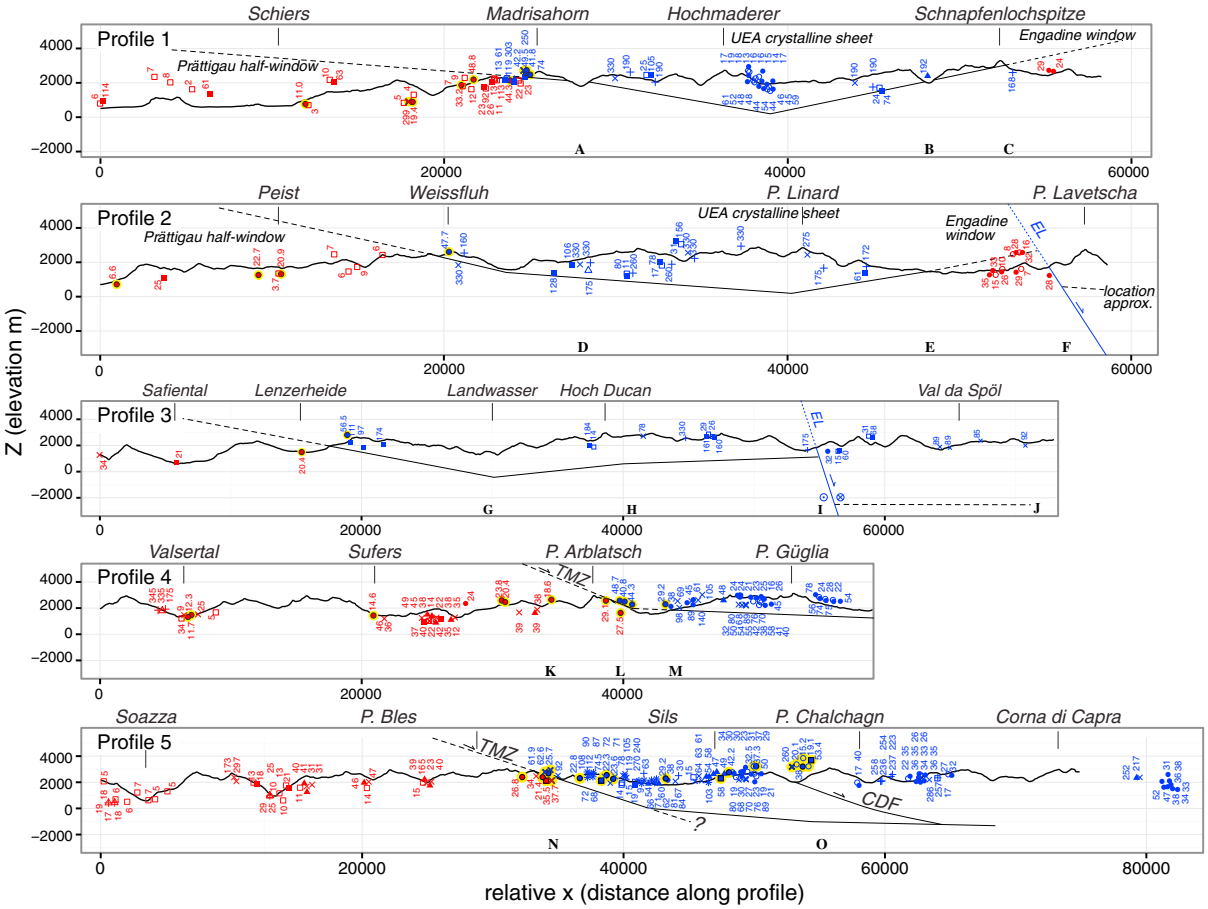

Figure 5. Profiles 1–5 as shown on the geologic map (Figure 4) with all samples projected into the sections according to their structural position. Structural-*Z* was measured orthogonally to the zero datum shown in each profile (positive is Austroalpine hanging wall; negative is Pennine footwall). Hanging wall samples are shown in blue; footwall samples in red; yellow highlighting indicates new ages from this study. Symbology is the same as in Figure 4. Note changes in length in the *x* axis, but there are no changes in scale across the sections. Constraints on the location and orientation of zero datum are listed and shown on profiles with bold capital letters underneath the location of the constraints as follows: A: Gargellen window. B: Jamtal window. C: three-point problem, 12° west apparent dip. D: Austroalpine contact at Klosters at 1,600 m elevation requires contact east of Davos to be above ~1,000 m elevation, possibly as high as 1,500 m elevation. E: three-point problem, 10° west apparent dip. F: apparent dip of 57° SE on Engadine normal fault is evident in Google Earth and on 1:25,000 scale Swisstopo geologic maps. G: base of Austroalpine crystalline sheet located from Schmid et al. (1996). H: Austroalpine crystalline sheet approximately 2 km thick as depicted by Schmid et al. (1996). I: apparent dip of 75°SE on Engadine scissor fault as depicted by Schmid et al. (1996). J: 5+ km thick sheet to base of Margna as depicted by Schmid et al. (1996). K: 22° dip on Turba mylonite zone at north end near Bivio as depicted by Nievergelt et al. (1996). L: dip slope of Piz Arblatsch as measured in the field. M: three-point problem, 5° east dip. N: Turba mylonite zone, 18° apparent dip in plane of section from Nievergelt et al. (1996). O: thickness of hanging wall is <3 km thick as depicted by Schmid et al. (1996).

neighboring transects, (4) using the axial surfaces of recumbent folds coring the major Pennine nappes (e.g., Niemet-Beverin fold) to constrain the orientation of the structural datum, and (5) making primary observations in the field. In addition, insofar as possible, our structural contacts conform to those found in the down-plunge projections of cross sections published by Schmid and Froitzheim (1993), Schmid et al. (1996), Scheiber et al. (2012), Milnes and Schmutz (1978), Schreurs (1993), Weh (1998), and Weh and Froitzheim (2001).

From north to south, Profile 1 is in the northern part of the northern half-window (Landquart Valley-Madrisahorn area) and contains samples from the northernmost exposures of the Pennine zone; its eastern-most part includes rocks from the Engadine Window. Profile 2 includes samples from the southern part of the northern half-window, generally between the towns of Chur and Davos. Profile 3 lies along the boundary between the northern and southern half-windows, between the towns of Lenzerheide to the west and the Zernez area of the Engadine Valley to the east. Profiles 4 and 5 transect the southern half-window. Profile 4 trends WNW, parallel to Profiles 1–3. Profile 5 trends ENE, intersecting Profile 4 near its eastern terminus at St. Moritz and ending near Passo del Bernina. A group of seven samples lie in the area between Profiles

3 and 4. These samples were included in Profile 4, but their vertical position was determined by the local exposure of the base of the Austroalpine allochthon rather than its projected position from the center of Profile 4, ~8 km to the south, which is at a substantially different structural elevation.

In the cross sections, the zero ($Z = 0$) structural datum is consistently defined at the bottom of the Arosa-Platta ophiolitic unit (or its local equivalent), generally corresponding to the Turba-Gürgaletsch fault zones as described above. Accordingly, the Schams-Falknis and Suretta nappes, Prättigau and Arblatsch flysch, North Penninic Bündnerschiefer, and Avers Bündnerschiefer represent the Pennine footwall, and the Arosa-Platta ophiolite, Tschirpen gneiss, and Austroalpine crystalline nappes (Margna, Sella, Err, Corvatsch, Bernina, Julier, Silvretta, Campo, and Grosina) and their respective Mesozoic cover represent the Austroalpine hanging wall.

The along-strike width of the zone of projection for each section is approximately 7 km (a few samples lie slightly outside of this), estimated to be small enough to avoid introducing significant (km-scale) errors in structural-*Z* (rectangular boxes in Figure 4). Sample positions were projected onto cross sections according to their true elevations (meters above sea level). In some cases (<15% of the database), owing to structural complexity, the projected structural position lay in a different structural unit on the section than its mapped position in the field. For these samples, structural-*Z* was adjusted up or down by a few tens to a few hundred meters, as required to place the sample in the proper tectonic unit. Sample elevations were generally not provided in the original references and thus were assigned to every sample in the published data set using the Advanced Spaceborne Thermal Emission and Reflection global digital elevation model, which has errors in elevation of approximately 10 to 25 m. By assigning every published sample an elevation-*z* coordinate from this single data source, a consistent elevation is applied across the data set. Samples from this study were assigned an elevation according to the *x*, *y* position as defined on 1:25,000 scale topographic maps published by SwissTopo (Landeskarte der Schweiz). On Profile 1, in the northern half-window, the strike of the base of the allochthon changes from north to northwest, requiring a cluster of ages from Weh (1998) to be elevated 500 m to be situated in their correct structural-*Z* position. Likewise, near the eastern terminus of Profile 4, due to nonplanarity of the base of the allochthon, a cluster of ages near Piz d'Err from Evans (2011) were adjusted downward about 800 m in structural-*Z*.

In addition to errors introduced by projecting perpendicular to the profiles, samples at the extreme east and west ends of the profiles with large values of structural-*Z* (either positive or negative) have relatively uncertain vertical position. For example, a cluster of samples from Campo-Grosina (Evans, 2011) that lie east of Profile 5 are too far from exposures of the base of the allochthon or any other structural datum to be assigned a credible structural-*Z* by projection (Figure 4). Thus, they were assigned a moderate structural-*Z* of about 5.5 km, which is approximately equal to that of the Bernina nappe.

The structurally lowest samples in the data set come from the Adula nappe at the western terminus of Profile 4, and the structurally highest samples come from the Bernina nappe at the eastern terminus of Profile 5, yielding a total vertical structural relief of approximately 22 km. This structural thickness is similar to values depicted in regional cross sections painstakingly constructed by down-plunge projection of the Pennine nappe stack (e.g., Milnes & Pfiffner, 1980; Schmid et al., 1996; Schreurs, 1993).

3.4. Methods

3.4.1. Mineral Separation

Mineral separates were made using the conventional steps of pulverization, washing, and sieving, followed by magnetic and heavy-liquid separation. For apatite and zircon, separates were concentrated prior to magnetic separation using a gold panning technique. Because separates obtained using this technique included a large fraction of 20 μm (length) grains, the recovery of the coarser grains in the separate used for analysis was likely >90%. The gold panning step reduced sample volume to <20 mL, greatly expediting magnetic and heavy-liquid separation. For white mica separates, multiple steps at progressively higher amperage were used for magnetic separation. Afterward, grains that adhered to coarse paper ("paper shake" method) were sieved at −250, −180, and −125 μm and then handpicked under a 50X binocular microscope. All samples analyzed for $^{40}Ar/^{39}Ar$ were −250/+125 μm in size, and preference was given to the coarsest size fraction that was also optically free from inclusions and defects.

3.4.2. Analytical Methods

The $^{40}Ar/^{39}Ar$ analyses were performed at the U.S. Geological Survey (USGS) in Denver, Colorado. Together with grains of the $^{40}Ar/^{39}Ar$ standard Fish Canyon sanidine, samples were irradiated for 7 MWH in the

central thimble position of the USGS TRIGA reactor (Dalrymple et al., 1981), while also being rotated at 1 rpm. Cadmium foil was used during the irradiation to prevent unwanted ^{40}Ar produced from ^{40}K. Following irradiation, the samples and standards were loaded with tweezers to a stainless steel sample holder and then placed into a laser chamber with an externally pumped ZnSe window. The reported incremental heating data represent results from 1 to 3 individual mineral grains. The volume of the mostly stainless steel vacuum extraction line, including a cryogenic trap operated at −130°C and two SAES™ GP50 getters (one operated at room temperature (0 A), one operated at 2.2 A), is estimated to be 450 cm^3. A combination of turbo molecular pumps and ion pumps maintain steady pressures within the extraction line of $<1.33 \times 10^{-7}$ Pa. Samples were incrementally heated in steps of 90 s, by controlled power output of a 50 W CO_2 laser equipped with a beam homogenizing lens resulting in uniform energy over the entire sample surface. During laser heating, any sample gas released was exposed to the cryogenic trap and was further purified for an additional 120 s by exposure to both the cryogenic trap and the SAES™ getters. The sample gas was expanded into a Thermo Scientific ARGUS VI™ mass spectrometer, and argon isotopes were analyzed simultaneously using four Faraday detectors (^{40}Ar, ^{39}Ar, ^{38}Ar, and ^{37}Ar) and one ion counter (^{36}Ar). Following data acquisition of 10 min, time zero intercepts were fit to the data (using parabolic and/or linear best fits) and corrected for backgrounds, detector intercalibrations, and nucleogenic interferences. The *Masspec* computer program written by A. Deino of the Berkeley Geochronology Center was used for data acquisition, age calculations, and plotting. All of our reported ^{40}Ar/^{39}Ar ages are referenced to an age of 28.201 ± 0.046 Ma for the Fish Canyon sanidine (Kuiper et al., 2008), the decay constants of Min et al. (2000), and an atmospheric ^{40}Ar/^{36}Ar ratio of 298.56 ± 0.31 (Lee et al., 2006). Laser fusion of >10 individual Fish Canyon Tuff sanidine crystals at each closely monitored position within the irradiation package resulted in neutron flux ratios reproducible to ≤0.25% (2σ). Isotopic production ratios were determined from irradiated CaF_2 and KCl salts, and for this study the following values were measured: (^{36}Ar/^{37}Ar)Ca = (2.48 ± 0.10) × 10^{-4}; (^{39}Ar/^{37}Ar)Ca = (1.22 ± 0.10) × 10^{-3}; and (^{38}Ar/^{39}Ar)K = (1.29 ± 0.03) × 10^{-2}. Cadmium shielding during irradiation prevented the formation of any measurable (^{40}Ar/^{39}Ar)K. ^{40}Ar/^{39}Ar plateau ages (and uncertainties) are considered the best estimate of the cooling age of the minerals and were calculated from samples if three or more consecutive heating steps released ≥50% of the total ^{39}Ar and also had statistically (2σ) indistinguishable ^{40}Ar/^{39}Ar ages.

Zircon fission track analyses were performed by Apatite to Zircon, Inc. Zircon grains from the Fish Canyon Tuff (Naeser locality) U-FT and U-Pb age standard, and zircon grains from the unknown samples were mounted in FEP Teflon, polished to expose internal grain surfaces at a minimum depth of about 20 μm, and etched for 36–72 h in a eutectic melt of NaOH-KOH to expose natural fission tracks for viewing using an optical microscope. Etched zircon grains were viewed using a Nikon Optiphot2 optical microscope affixed with a 100X dry objective and a Lumenara Infinity 2 1,600 × 1,200 pixel color digital camera, aided by an Applied Scientific Instrumentation MS-2000 XY stage and Applied Scientific Instrumentation *Z*-Axis drive. Fission track counting was done after laser ablation-inductively coupled plasma–mass spectrometry (LA-ICP-MS), by R. Donelick, on a computer display screen, using previously collected image stacks, and in the vicinity of the laser ablation pit, a view of which was visible during counting (Donelick et al., 2005). Zircon grains selected for fission track age dating, including Fish Canyon Tuff zircon for fission track age calibration, were analyzed by LA-ICP-MS during two sessions (ZFTUPb_13_06_08 and ZFTUPb_13_06_20) to determine uranium concentrations for fission track age calculation and U-Pb ages for selected areas for which fission tracks were counted.

Apatite (U-Th)/He analyses were completed at the California Institute of Technology. ^{4}He was measured on a Pfeiffer Prisma quadrupole mass spectrometer using isotope dilution methods referenced to calibrated quantities of ^{3}He. Concentrations of U and Th were measured on an Agilent 7500 inductively coupled plasma–mass spectrometer using a ^{232}Th/^{235}U spike. The run was standardized using Durango fluorapatite that has a long-term measured mean cooling age of 32.0 ± 1.0 Ma (Farley, 2002).

One round of (U-Th)/He zircon analyses were split such that ^{4}He concentrations were measured on a quadrupole mass spectrometer at Caltech (same as for apatite (U-Th)/He above), and U, Th, and Sm concentrations were measured at the University of Colorado Boulder in the CU TRaIL facility. This "split" analysis affected three grains in the current study (110830-03, 110825-03, and 110825-14). The rest of the (U-Th)/He zircon analyses were done completely at the University of Colorado Boulder using the following method: Individual mineral grains were handpicked using a Leica M165 binocular microscope equipped with a calibrated

digital camera and capable of both reflected and transmitted, polarized light. We selected grains >60 μm in width and with various morphologies and/or clarities to improve the likelihood of selecting grains with a variety of effective uranium (eU) concentrations. Individual grains were measured twice for length and width, the dimensions of which define the "spherical equivalent radius," packed into Nb tubes, and loaded into an ASI Alphachron He extraction and measurement line. The packet is placed in the UHV extraction line (~3×10^{-8} torr) and heated with a 25 W diode laser to 800–1100°C for 5 to 10 min to extract radiogenic ^{4}He. The degassed ^{4}He is then spiked with approximately 13 fm^3 of pure ^{3}He, cleaned via interaction with two SAES getters, and analyzed on a Balzers PrismaPlus QME 220 quadrupole mass spectrometer. This procedure is repeated at least once to ensure complete mineral degassing. Degassed grains were then removed from the line, and taken to a Class 10 clean lab for dissolution.

Zircon is dissolved using Parr large-capacity dissolution vessels in a multistep acid-vapor dissolution process. Grains encased in a Nb tube are placed in Ludwig-style Savillex vials, spiked with a ^{235}U-^{230}Th tracer, and mixed with 200 μL of Optima grade HF. The vials are capped, stacked in a 125 mL Teflon liner, placed in a Parr dissolution vessel, and baked at 220°C for 72 h. After cooling, the vials are uncapped and dried down on a 90°C hot plate until dry. The vials then undergo a second round of acid-vapor dissolution, this time with 200 μL of Optima grade HCl in each vial that is baked at 200°C for 24 h. Vials are dried down a second time on a hot plate. Once dry, 200 μL of a 7:1 HNO_3:HF mixture is added to each vial, the vial is capped, and heated on the hot plate at 90°C for 4 h. Final solutions are diluted with 1 to 3 mL of doubly deionized water and taken to the ICP-MS lab for analysis. Sample solutions, along with normal solutions and blanks, are analyzed for U, Th, and Sm content using a Thermo Element 2 magnetic sector mass spectrometer equipped with a Teflon spray chamber and platinum cones. Once the U, Th, and Sm concentrations have been measured, He age dates and all associated data are calculated using the methods described in Ketcham et al. (2011). Every batch of samples includes standards run sporadically throughout the process to monitor procedures and maintain consistency from run to run. Long-term averages of Fish Canyon Tuff zircon and Durango fluorapatite run in the CU TRaIL facility are 28.7 ± 1.8 Ma (n = 150) and 31.1 ± 2.1 (n = 85), respectively.

3.5. Data

The thermochronological results from this study (Table 2; Supplementary Information; Price et al., 2017) broadly overlap previously published ages when plotted as a function of structural position versus age (Figure 6). Both data sets define a sideways "L" shape, where the short limb represents a narrow range of relatively young (Tertiary) ages in the Pennine footwall, and the long limb represents a broad span of older (late Paleozoic to mid-Tertiary) ages in the Austroalpine hanging wall. As a rule, the new ages reported in Table 2 for any given mineral system confirm previous constraints on the thermal histories of both the hanging wall and footwall, but, critically, they extend these constraints to a structural position much closer to their respective boundaries, facilitating an assessment of whether thermal histories adjacent to the fault are similar or different to one another, and similar or different to the thermal histories in the respective structural cores of the Penninic and Austroalpine realms. We present the data in three basic forms: (1) simple plots of age versus geographic coordinates (easting, northing), (2) age versus our estimates of relative structural position (structural-Z), and (3) subsets of ages from key mineral systems in hanging wall and footwall that are closest to the base of the Austroalpine allochthon ("pincher" plots).

We plot age versus geographic coordinate according to the 1903 Swiss Grid (Figures 7 and 8 for north-south and east-west cross-sectional views) following the convention in Figure 4 and used in all subsequent plots (fission track ages are squares; (U-Th)/He ages are circles; closed for zircon, open for apatite; Rb-Sr ages are triangles, open for biotite, closed for white mica; Ar ages are asterisks (amphibole), 'x's (white mica), and plus signs (biotite), colored red for footwall and blue for hanging wall). The plots in Figures 7 and 8 include a composite showing data for all mineral systems (frame A), a plot discriminating previously published ages from the new ages presented here (frame B), and plots showing subsets of data according to (U-Th)/He, fission track, and Ar systems (frames C, D, and E, respectively).

A few general trends are evident in the data. The first is that, in the (U-Th)/He plot looking east (Figure 7c), the hanging wall and footwall ZHe ages are separable into older and younger populations by an approximately linear boundary with a slope of 0.27 Myr/km. This line is mainly defined by a northern cluster of hanging wall ages of ≥40 Ma at 200,000N (latitude in middle of Prättigau half-window), a southern cluster of hanging wall

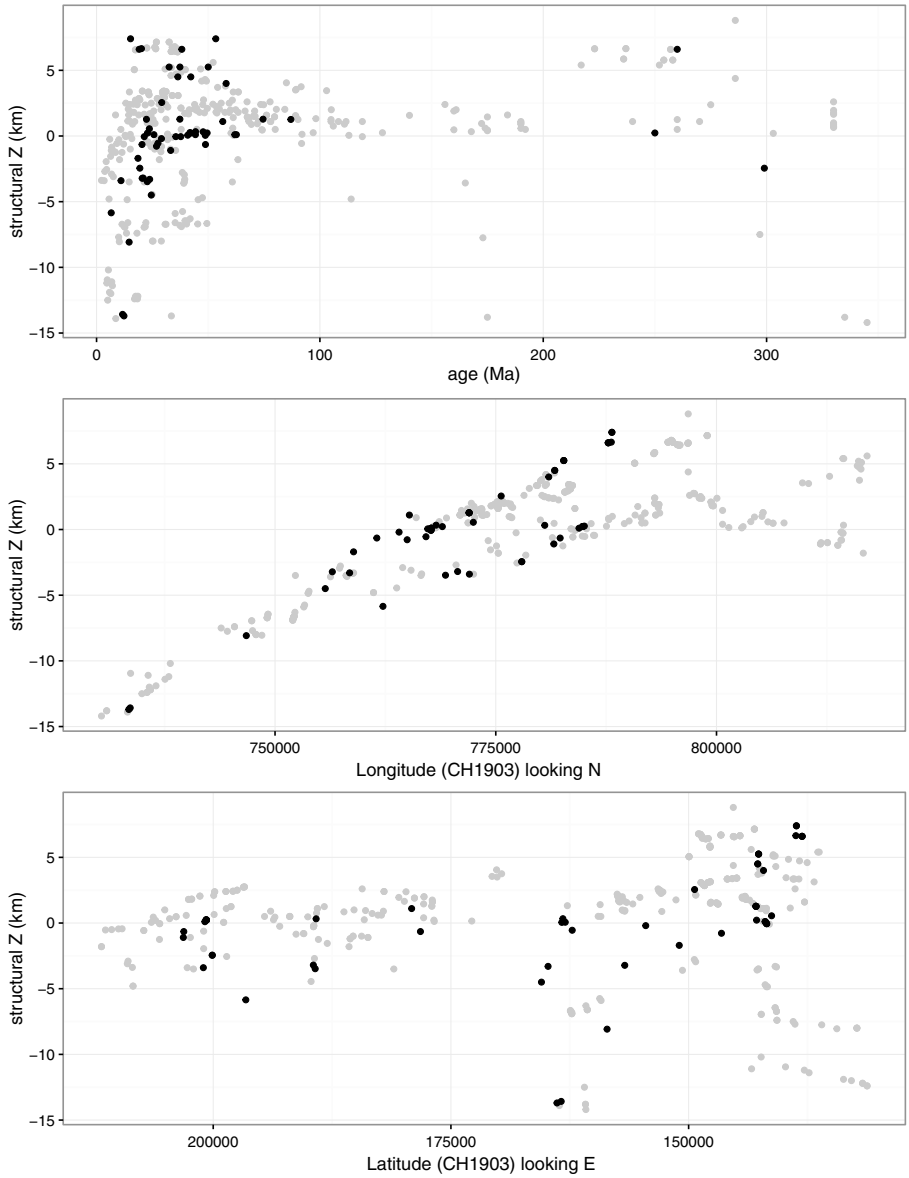

Figure 6. Structural-*Z* versus age, longitude, and latitude. New sample locations are colored black; published sample locations are gray. Locations where black dots do not overlap gray dots are unique sample locations from this study.

ages of ≥29 Ma at 149,000N (latitude of St. Moritz), and the broad distribution of footwall ages between 180,000N and 140,000N that lie below the line. Out of a population of 102 ages total, only one footwall ZHe age plots above the line, at the far northern end of the study area (at the latitude of the Madrisahorn), and three hanging wall ZHe ages plot below the line at the southern end of the study area (at the latitude of Maloja Pass). Across the entire width of the (U-Th)/He plot (Figure 7c), footwall ZHe ages persistently overlap hanging wall AHe ages.

A second noteworthy trend is observed in the fission track data (Figure 7d), in which an array of the youngest hanging wall ZFT ages, ranging from 61 Ma in the north to 53 Ma in the south, define a line of slope 0.11 Myr/km. Across the southern three quarters of the study area, a line of similar slope of 0.10 Myr/km is defined by an array of eight footwall ZFT ages ranging from 18 to 25 Ma. There is one outlier to this trend with an age of 36 ± 12 Ma at the southern end of the section, which in any event has error nearly an order of magnitude greater than any point in the trend. In the northern one quarter of the section (at the latitude of the northern half-window), footwall ZFT ages are much older and concordant with the hanging wall ZFT ages, ranging

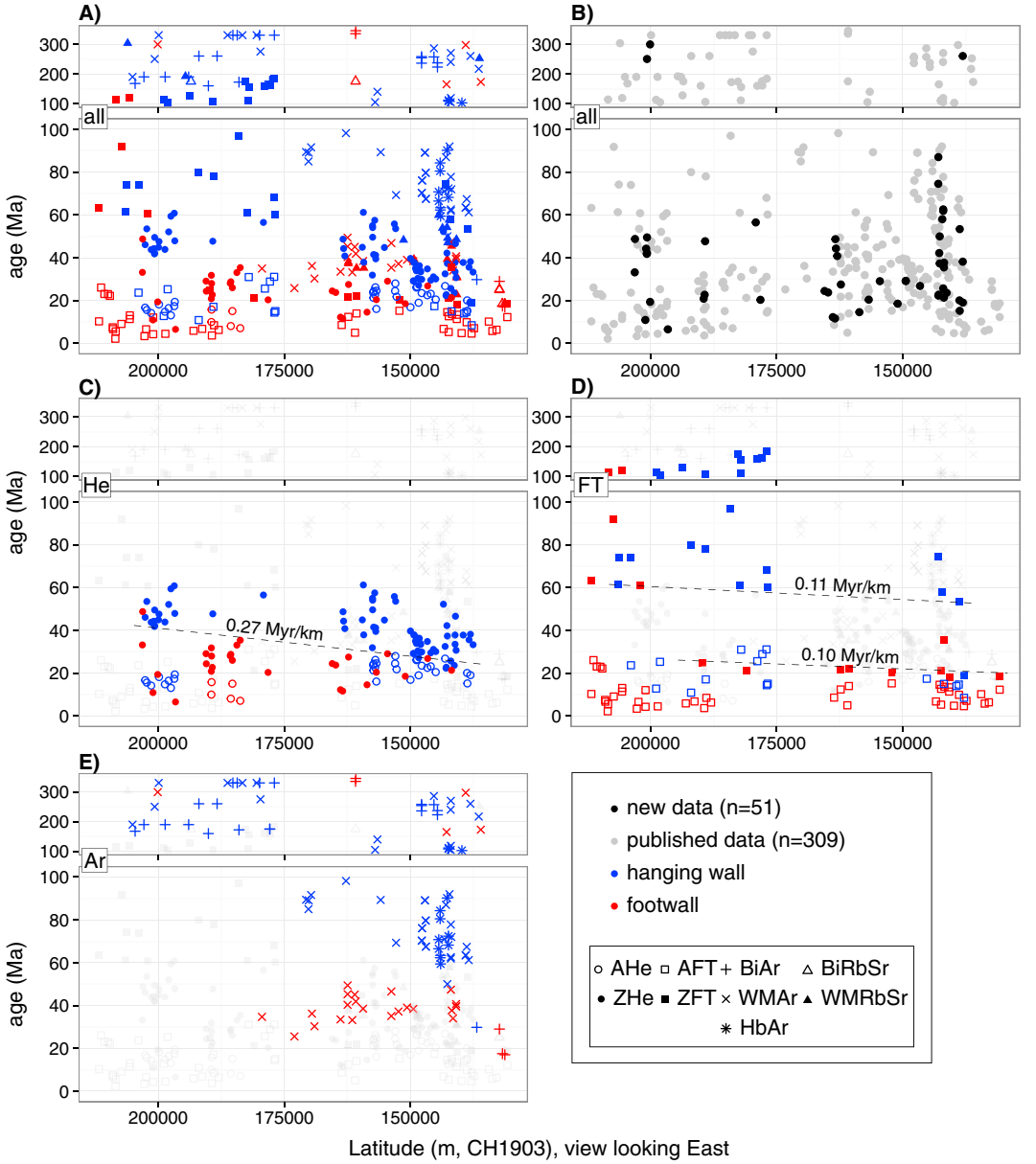

Figure 7. Plots of cooling age versus latitude, view looking east, for all data (new and published, $n = 360$) compiled for this study. (a) Combined new and published thermochronometric data, symbology for thermochronometric systems shown in key; in this and subsequent plots, blue represents hanging wall; red represents footwall. (b) New (black) and published (gray) thermochronometric data. (c) Subset of all (U-Th)/He data, zircon: closed circles and apatite: open circles. Dashed lines are age gradients discussed in text. (d) Subset showing all fission track data, zircon: closed boxes and apatite: open boxes. (e) Subset showing all K/Ar and Ar/Ar data, plus sign: biotite, letter-x: white mica, and asterisk: hornblende. Table of data supporting these plots is found in the supporting information and in the EarthChem database.

from 61 to 119 Ma. Between the two trends, there is a temporal gap between footwall and (minimum) hanging wall ZFT age of 36 Myr that persists for at least 60 km across orogenic strike.

A third trend is observed in the Ar mica ages (Figure 7e) in which the population of ages younger than 100 Ma are strongly bimodal, with one mode ranging from 60 to 98 Ma corresponding to the hanging wall and a second mode ranging from 18 to 49 Ma corresponding to the footwall. With one notable exception, there is an absence of Ar-mica ages between 50 and 60 Ma. The range of hanging wall ages dramatically expands from north to south. Ages in the north are consistently Jurassic or older (150–330 Ma), whereas ages in the central part of the section are as young as 80 Ma and, in the southernmost part of the section, as young as 60 Ma. In

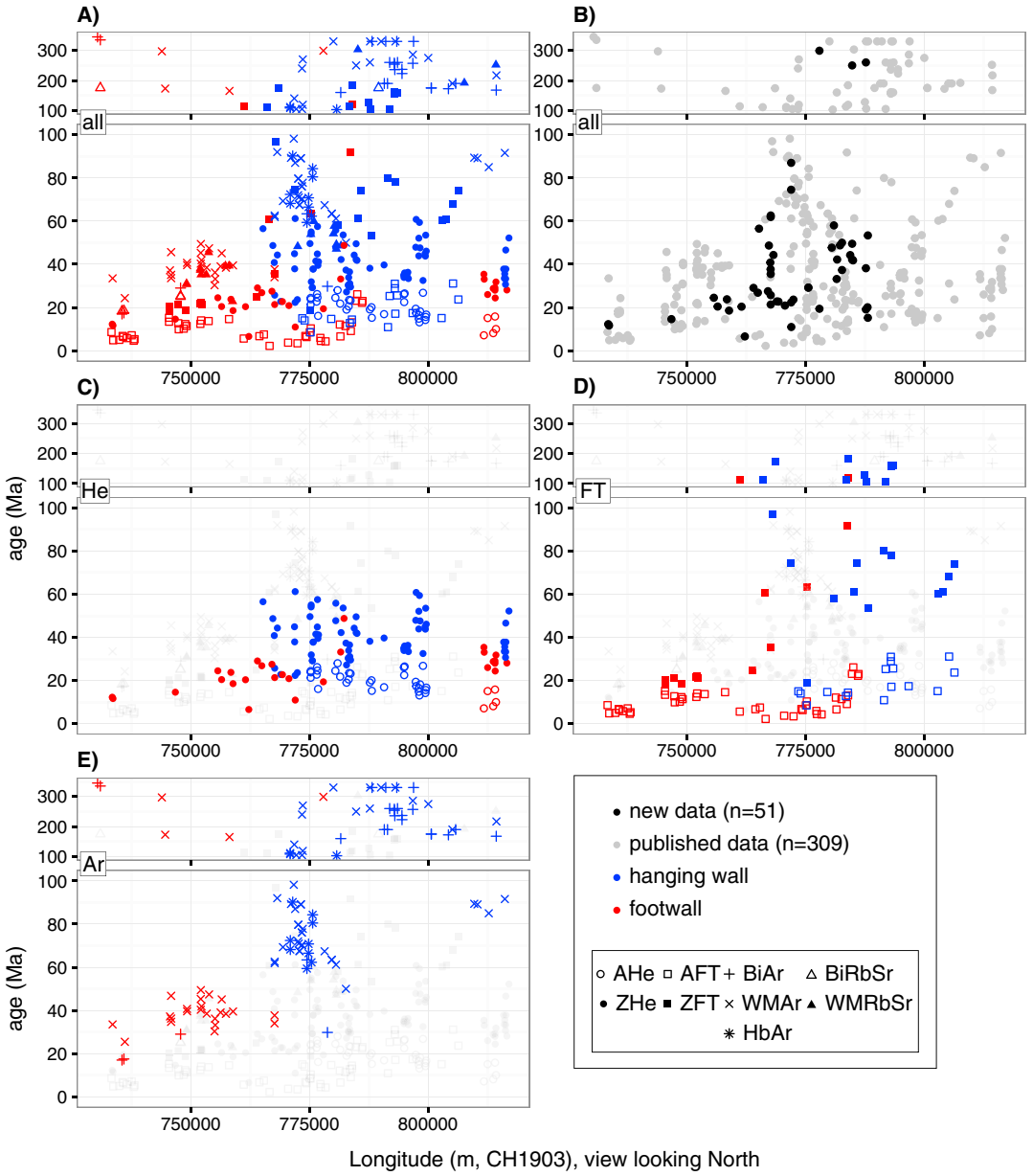

Figure 8. Plots of cooling age versus longitude, view looking north, for all data (new and published, $n = 360$) compiled for this study. (a) Combined new and published thermochronometric data, symbology for thermochronometric systems shown in key; in this and subsequent plots, blue represents hanging wall; red represents footwall. (b) New (black) and published (gray) thermochronometric data. (c) Subset of all (U-Th)/He data, zircon: closed circles and apatite: open circles. (d) Subset showing all fission track data, zircon: closed boxes and apatite: open boxes. (e) Subset showing all K/Ar and Ar/Ar data, plus sign: biotite, letter-x: white mica, and asterisk: hornblende. Table of data supporting these plots is found in the supporting information and the EarthChem database.

addition to these patterns, the total age population in the footwall is strongly split between the Tertiary population and a smaller population that ranges from Paleozoic to Jurassic. There is a complete absence of <50 Ma Ar ages north of 179,000N (latitude of Lenzerheide). In the hanging wall, with one notable exception, there are no K/Ar ages younger than 60 Ma north of 138,000N.

The systematic geographical trends apparent in the north-south latitudinal section (looking east) are not apparent in the east-west longitudinal section (looking north; Figure 8) indicating that most of the variation in cooling ages occurs across, rather than along, orogenic strike. However, there does appear to be, both in individual mineral systems and in the data set as a whole, a westward younging trend in footwall ages in the

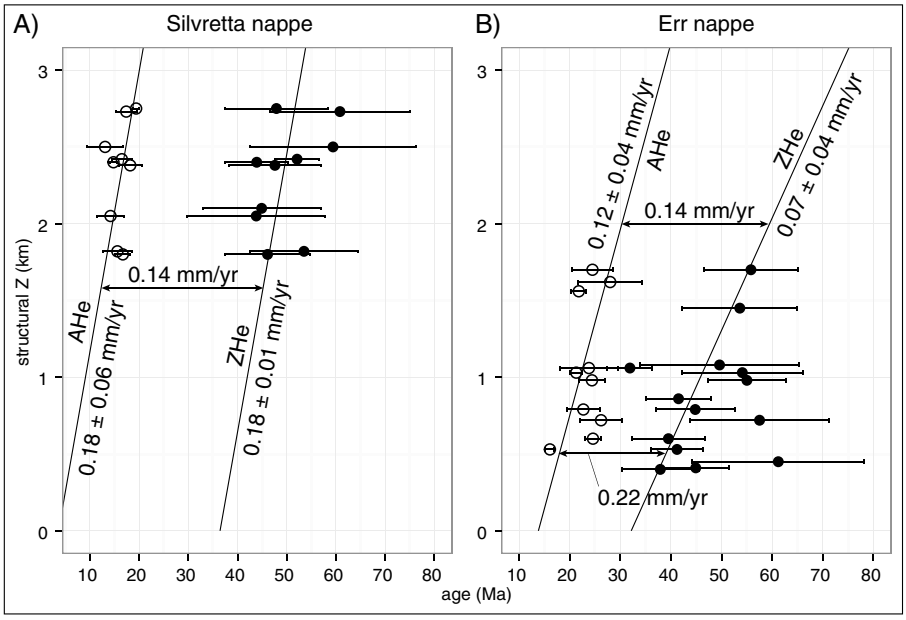

Figure 9. Structural-*Z* versus age for (a) Silvretta and (b) Err nappes using AHe and ZHe data from Evans (2011) fit with a weighted regression (York et al., 2004) that accounts for error in age (standard deviation of a population of single grain ages in a sample) and structural-*Z* (fixed ±0.2 km uncertainty). Both data sets indicate slow cooling and erosion rates of order 0.1–0.2 mm/yr through most of the Tertiary for large crystalline units of the Austroalpine allochthon, which is in general agreement with estimates made by Hurford et al. (1989) and Evans (2011).

western one third of the data set. For instance, near 750,000E, Ar-biotite, ZHe, and AFT ages are 30, 20, and 12 Ma, respectively, whereas near 730,000E, the same three systems record ages of 18, 12, and 5 Ma, respectively. As discussed above, the relatively strong variation in the westernmost ages likely reflects the occurrence and subsequent cooling after the circa 18 Ma Lepontine Barrovian metamorphism (Wiederkehr et al., 2009). In this projection, there is significant overlap between ZHe ages in hanging wall and footwall with no overall trend otherwise apparent in either population, with the exception of westward younging of footwall ZHe ages as just discussed.

Because we are fundamentally interested in the relationship of cooling history with respect to the base of the Austroalpine allochthon, we plot age against structural-*Z*. We assume that the post-Cretaceous cooling history of the hanging wall was almost exclusively the product of erosional unroofing, but leave open the possibility that footwall cooling resulted from both tectonic and erosional unroofing. For erosion rates of ~1 mm/yr or more, the rate of upward advection of heat becomes significant relative to conductive cooling (Péclet number $>$ 1; e.g., Figure 2.25 in Allen & Allen, 2006). For rates of ~0.5 mm/yr or less, advection is negligible, and hence the age gradient with structural depth is a rough estimate of the erosion rate. For any given mineral system, cooling ages will ideally young with structural depth. With age-structural-*Z* data on multiple mineral systems, there are two quasi-independent methods to estimate the rate of descent of isotherms through the crust. The first is simply age variation with depth; the second are differences in age between mineral systems in samples at the same depth. In the latter case, the change in temperature with time can be converted to change in depth with time if a geothermal gradient is assumed.

Linear regression (York et al., 2004) of depth profiles for ZHe and AHe ages from two crystalline nappes in the hanging wall, Silvretta and Err (Figure 9; ages and locations shown in Figures 4 and 5), yield slopes of 0.18 ± 0.01 mm/yr for Silvretta-ZHe, 0.18 ± 0.06 mm/yr for Silvretta-AHe, 0.07 ± 0.04 mm/yr for Err-ZHe, and 0.12 ± 0.04 mm/yr for Err-AHe. For weighting purposes, error in the ordinate is qualitatively estimated to be 0.2 km for structural-*Z*, whereas error in the abscissa is the standard deviation (1σ) of the population of single grain ages for a given sample. For Silvretta (Figure 9a), the difference in ZHe and AHe age as a function of depth is essentially invariant and yields a gradient d*Z*/d*t* of 0.14 mm/yr, assuming a 25°C/km geothermal gradient. In contrast, for Err (Figure 9b), the ZHe and AHe gradients vary in age as a function of depth and

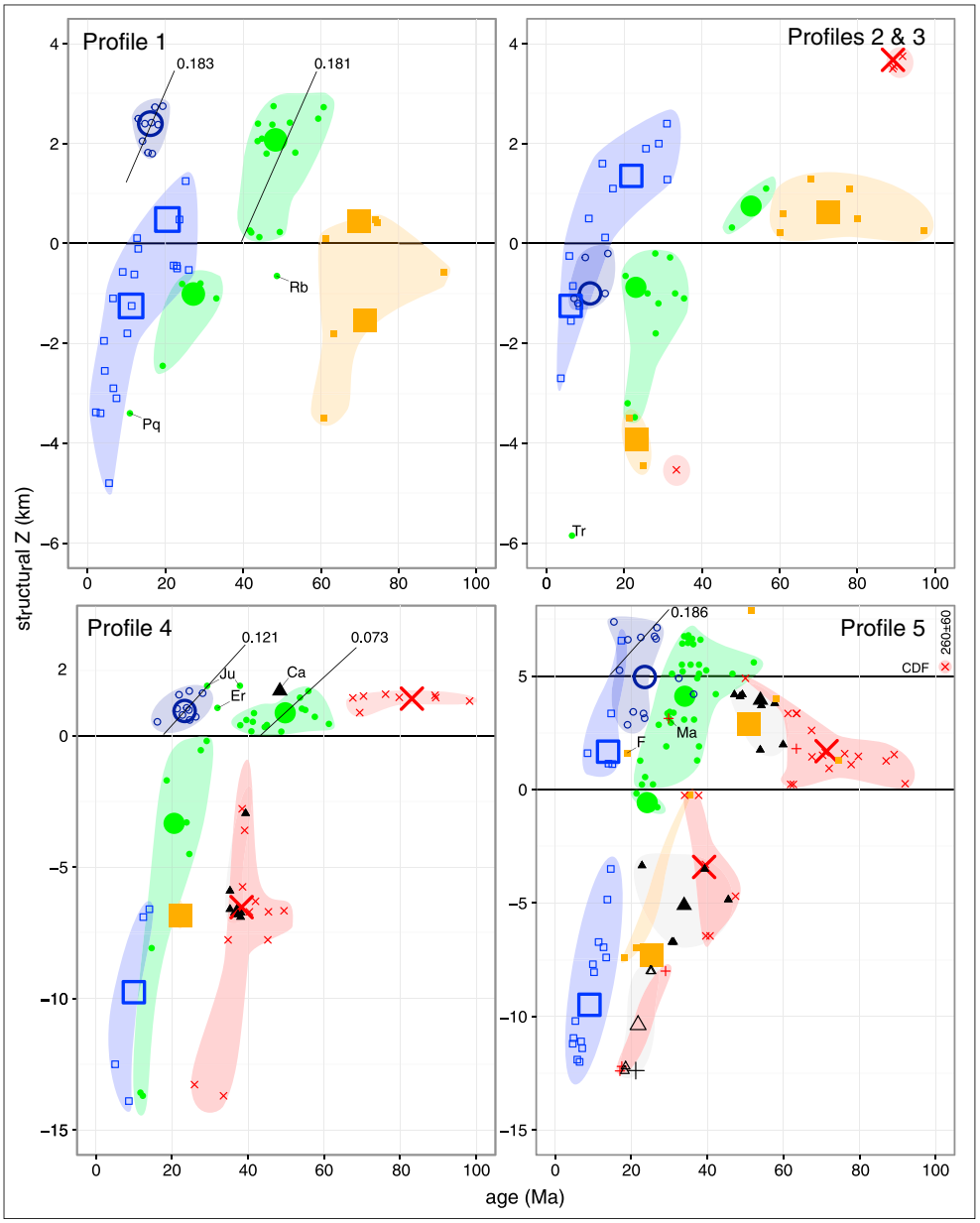

Figure 10. Structural-*Z* versus age plots constructed from the five profiles defined in Figures 4 and 5. Raw data are shown as points using the symbology from Figures 4, 7, and 8. Shaded transparent areas are qualitative regions encompassing a given thermochronometric system, and the same color is used for hanging wall and footwall. Blue squares: AFT, dark purple open circles: AHe, green closed circles: ZHe, orange closed boxes: ZFT, black open triangle: Rb/Sr biotite, black closed triangle: Rb/Sr white mica, red plus sign: K/Ar or Ar/Ar biotite, and red letter-x: K/Ar or Ar/Ar white mica. Enlarged points represent average age at median structural-*Z*. Profiles 2 and 3 have been combined since they cover similar geologic terrain and have a paucity of data in certain key cooling systems. Best-fit weighted regression lines (viz., Figure 9) are shown for certain hanging wall nappes. Outliers to the general trends are labeled: Ca: Carungas, F: Forno, Ju: Julier, Ma: Margna, Pq: Pragmartin quarry (Bündnerschiefer), and Rb: Ruchberg (Prättigau flysch). Corvatsch detachment fault (CDF) shown at +5 km structural-*Z* in Profile 5.

decrease proportional to structural-*Z*, yielding an approximate d*Z*/d*t* of 0.14 mm/yr at 2 km structural-*Z* and 0.22 mm/yr at 0.5 km structural-*Z*. We interpret the regressions from Err and Silvretta ZHe and AHe data to be representative of the Austroalpine hanging wall as a whole and posit that the sheet has an average long-term exhumation rate of ~0.1–0.2 mm/yr from Paleogene to Neogene time. Our estimate is consistent with estimates made for the Silvretta nappe by Hurford et al. (1989) using AFT ages, for the Err nappe by Evans

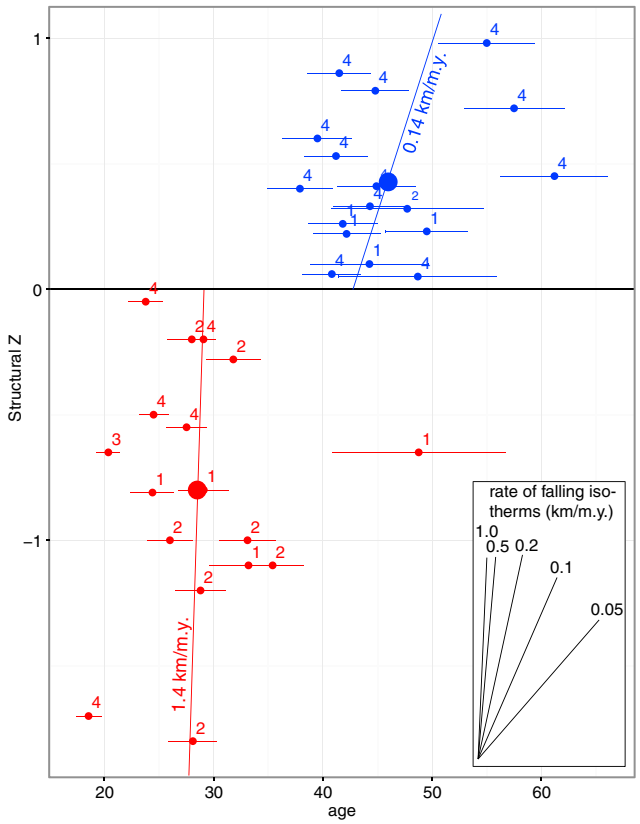

Figure 11. Composite plot of subset of ZHe ages for samples <1 km above the fault for the Austroalpine hanging wall and <2 km below the fault for the Pennine footwall extracted from Profiles 1–4 (points numbered according to profile). Large dots show mean age of the data sets plotted at the median structural depth. Slopes through the large dots represent nominal vertical age gradients (see discussion in main text) and are not formal regressions through the data.

(2011) using HeMP modeling of ZHe and AHe ages, and for the Silvretta nappe by Evans (2011) using raw thermochronometric ages.

In contrast to the broad spectrum of ages and discernible positive age-elevation slopes in some subsets of data in the hanging wall, ages in the footwall are both more tightly clustered and show comparatively little variation in age with structural depth. For example, for subsets of data with a reasonably large depth range, ages do not vary by more than 10 Myr over nearly 10 km of total structural depth, yielding slopes corresponding to exhumation rates ≥1.0 mm/yr. HeMP modeling of Pennine footwall ages from the Engadine window yielded an exhumation rate of ~1.7 mm/yr during the time period 52–38 Ma (Evans, 2011).

As presented in the format of Figures 7 and 8, relationships between structural features and cooling ages are not obvious, except as might be suggested by gross differences in age between hanging wall and footwall samples. To quantitatively address these differences, we present a subset of ages (0–100 Ma), colored by thermochronometric system, plotted versus structural-Z (Figure 10). In general, for mineral systems with closure temperatures of ZHe (180°C) or higher, all profiles show distinct discontinuities between hanging wall and footwall cooling ages at $Z = 0$, with age differences of a few tens of million years. In contrast, for systems with closure temperatures of AFT (110°C) or lower, no age discontinuity is apparent at $Z = 0$ or elsewhere. Two exceptions to this general pattern are the ZFT system on Profile 1 and the ZHe system on Profile 5 where no age discontinuity is apparent at $Z = 0$. However, there is an indication that an additional discontinuity exists at approximately +5 km structural-Z associated with the Corvatsch detachment fault (CDF in Profile 5, Figure 10; also termed "Corvatsch normal fault" by Schmid et al., 1996 and "Corvatsch mylonite zone" by Nievergelt et al., 1996, and Liniger, 1992, who also places a normal fault arrow on the zone), particularly defined by a pair of disparate $^{40}Ar/^{39}Ar$ white mica ages above and below that fault.

Of the 360 ages used in our study, only nine outliers (2.5%) do not conform to the general cooling pattern and are labeled individually on Figure 10. For the ZHe system, they include one relatively old footwall age from the Lower Tertiary Ruchberg Formation (Rb) in Profile 1, two relatively young footwall ages from Bundnerschiefer at the Pragmartin quarry (Pq) in Profile 1 and at Trimmis (Tr) in Profile 2, and three relatively young hanging wall ages in crystalline rocks of the Err nappe (Er) and Julier granite (Ju) on Profile 4. In terms of the total population of ZHe ages represented in Figure 10, labeled outliers represent 3/28 (10.7%) of the footwall subset, whereas labeled outliers represent 3/69 (4.3%) of the hanging wall subset. Other data outliers include one young Rb/Sr white mica age from the Carungas nappe (Ca) in Profile 4, one young ZFT age from the Forno unit (F) and one young K/Ar biotite age from the Margna nappe (Ma), both in Profile 5. Given the very small representation of these outliers in the data set, we ignore them in our analysis and interpretation of the data.

3.6. Geographic Pattern of Mid-Tertiary Cooling

Perhaps the most significant pattern, other than the contrast in cooling history of the hanging wall and footwall, is the geographic pattern within the Austroalpine allochthon in ZHe ages as alluded to above. Rocks within a few kilometers above the base of the Austroalpine allochthon have ZHe ages of 40 to 50 Ma in Profiles 1 to 4, which decrease to 20 to 30 Ma in Profile 5, assuming the base of the allochthon corresponds to the Turba mylonite zone. For Profiles 1 to 4, there appears to be no systematic differences in ages of footwall samples within ~2 km of the top of the Pennine zone (Figure 10). From north to south across these transects, there is also no systematic trend in either footwall or hanging wall ZHe ages. Averaging the ages and projecting the mean age to the fault (structural-$Z = 0$), the footwall age is about 29 Ma and the hanging wall age is about 43 Ma, a gap of some 14 Myr (Figure 11).

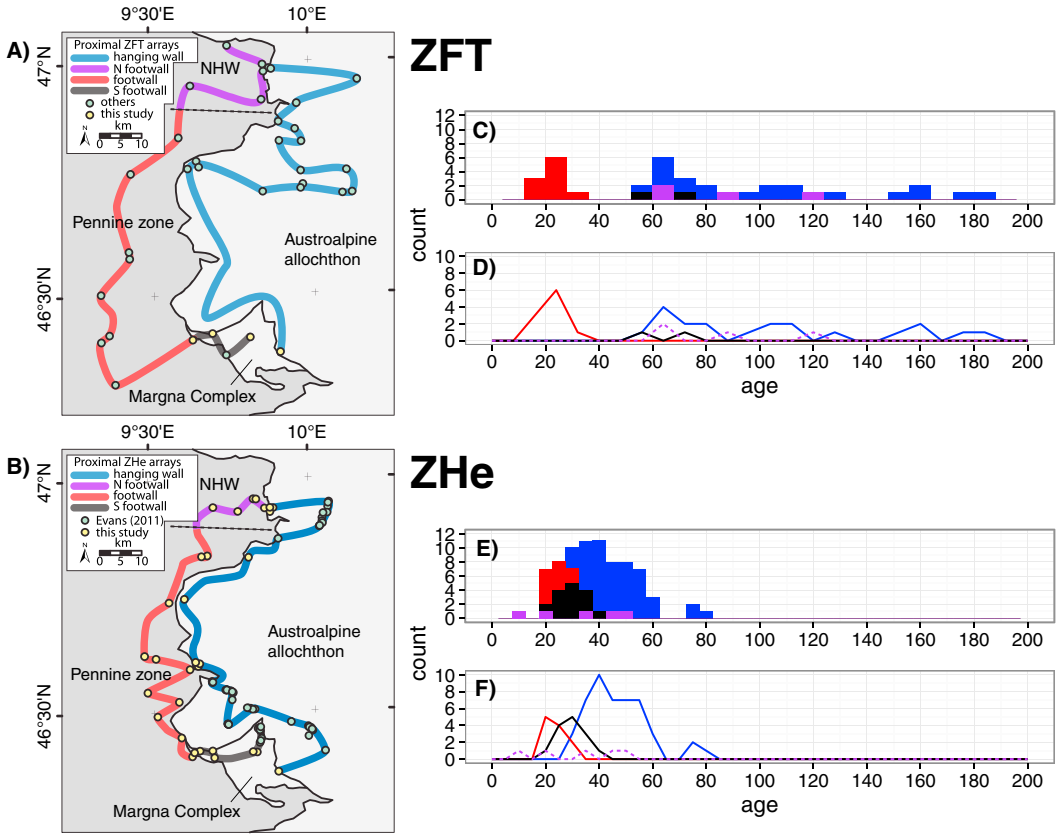

Figure 12. "Pincher" plots of age constraints on the Austroalpine allochthon from samples closest to the fault contact. (a, b) Location maps of ZFT and ZHe, respectively, ages. NHW: Northern half-window. (c, e) Stacked histograms of ZFT and ZHe, respectively, ages colored as per the legends in Figures 12a and 12b. (d, f) Frequency polygons of ZFT and ZHe ages, using the same data as in Figures 12c and 12d. Purple line has been dotted to improve legibility.

A second pattern is apparent in ZFT and ZHe age histograms for samples geographically adjacent to the boundary, which suggests the data are divisible into four geographical arrays (Figures 12 and 13): (1) the Austroalpine hanging wall, (2) the central portion of the Pennine footwall, (3) a cluster of ages at the north end of the Prättigau half-window, and (4) ages in the "Margna complex," an amalgamation that includes the Margna nappe and surrounding portions of the Platta and lowermost East Alpine nappes, including the Corvatsch "digitation" but excluding the Err and Bernina nappes. The Prättigau and Margna complex arrays are defined by distinctive age patterns in the footwall. In the former, footwall ZFT and ZHe ages increase and become similar to hanging wall ages (magenta points in Figures 12 and 13). In the latter, hanging wall ZHe ages decrease and become similar to footwall ages, whereas ZFT ages remain similar to the rest of the hanging wall (black points in Figures 12 and 13). Even though the Margna complex has Late Cretaceous-early Tertiary ZFT ages similar to the Austroalpine allochthon, it has much younger ZHe ages (consistently 22–30 Ma) than most of the Austroalpine allochthon (which is generally >35 Ma). This is seen in Profile 5 where the Margna complex age distribution overlaps the Austroalpine population at its upper end and the Pennine population at its lower end. Thus, the Margna complex appears to have a thermal history that requires a tectonic history that is distinct from both the Austroalpine allochthon and Pennine zone.

4. Discussion

The northern and southern extremes of the data set (Prättigau half-window and Margna complex) appear to be the "exceptions that prove the rule" that the hanging wall and footwall each yield a characteristic age pattern involving multiple thermochronometers and that the two patterns differ markedly. We return to the question posed earlier (section 2.4) of whether the contrast in ages between hanging wall and footwall resulted from erosion through an intact crustal section, or upward motion of heat across a crustal-scale

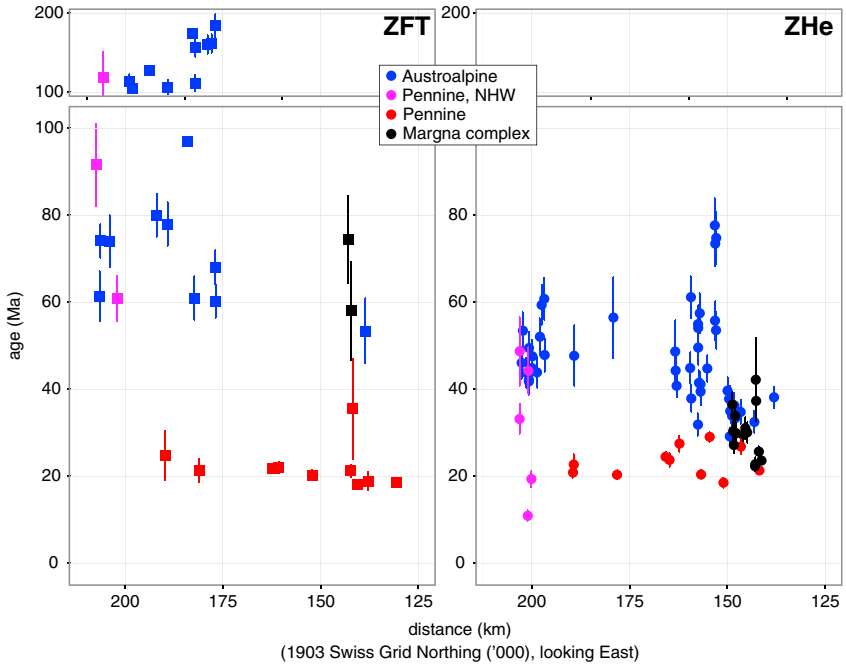

Figure 13. Age versus latitude subset showing a persistent gap in ages between the hanging wall and footwall, especially apparent in the ZFT data but still evident in the ZHe data between 150 and 190 km north. Color scheme shown in key is same as in Figure 12 (blue: hanging wall, red: footwall, and magenta: northern half-window (Profile 1); black: Margna complex).

fault. The data argue strongly in favor of the latter, both at the level of individual transects (Figure 10) and at the level of composite data sets for samples closest to the boundary (Figures 11–13). Below, we use these age patterns and petrologic depth constraints to estimate Tertiary temperature and depth histories of the hanging wall and footwall, and we speculate on their significance for the timing and mode of juxtaposition.

4.1. Model Thermal Histories

In modeling thermal histories, our goal is to estimate the first-order pattern using a traditional blocking temperature approach (e.g., Hurford et al., 1989), where each mineral system defines a closure event which records the downward passage of an isotherm at a particular time and place. This basic approach is justified, first, by the fact that constraints on the thermal history of the Austroalpine-Pennine boundary zone between 300°C (lowest closure temperatures of Ar/Ar and Rb/Sr mineral systems) and 70°C (AHe) are, to date, disparate, unpublished datasets from theses (e.g., Augenstein, 2012; Evans, 2011; Weh, 1998). Second, the large dataset that we have compiled for this study records, with considerable spatial and temporal redundancy, the relatively rapid descent through mineral closure temperatures of at least six key systems, which in descending order of closure at nominal cooling rates include Ar white mica (425°C), Rb/Sr biotite (300°C), ZFT (240°C), ZHe (180°C), AFT (110°C), and AHe (70°C) (Farley, 2002; Hunziker et al., 1992). Clearly, uncertainties in the thermal histories of the major rock masses can be better estimated by (1) multidomain diffusion modeling of K-feldspar, (2) closure temperature studies of individual grains, (3) numerical modeling of cooling curves (e.g., HeFTy), and (4) joint, multidimensional thermal modeling of heat conduction and mineral system diffusivity (e.g., Pecube, QTQt, and similar approaches). Nonetheless, we are confident that the signal of strongly contrasting thermal histories in the hanging wall and footwall are well enough defined by both sample distribution and reproducibility of individual ages that a simple "nominal closure event" approach is sufficient to address the fundamental issue of the timing and kinematics of juxtaposition of the Austroalpine allochthon and Pennine zone.

The first-order pattern of the data set (Figures 10–13) indicates that any differences that may exist within either the Austroalpine or Pennine masses adjacent to the boundary, except at the extreme northern and southern limits of its exposure, are negligible in comparison to the difference observed between the masses. The lower age versus structural-*Z* gradients in, and wider spacing of ages between, systems in the hanging

wall versus the footwall both indicate earlier, slower cooling of the hanging wall. We therefore assume that below ~300°C each plate cooled monotonically, such that each mineral system experienced a single closure event at a certain time in the hanging wall and footwall of each profile area. We also assume that within each plate, temperature varied with structural-*Z* at a rate of 25°C/km.

We estimate the closure event to have occurred at the mean age for each mineral system in each plate and each profile of the data set and estimate the depth (structural-*Z*) of the event to be the median depth of the sample set for a given system. We then account for vertical variation in the time of closure events using our estimated age gradients converted to depth (Figures 9 and 10), which yield 0.1 to 0.2 mm/yr in the hanging wall and 1.0–1.5 mm/yr in the footwall. The precise choice of geothermal gradient (e.g., 20°C/km versus 25°C/km) introduces proportionate error in our conversion of temperature to depth, but the error is small (~20%) in comparison to the range of possible age gradients (which vary by more than a factor of 2). We note that despite this relatively large uncertainty, the scaling between the gradients and total vertical variation in the sample set introduces only a small error in assigning a precise depth for a given closure event. For 0.1–0.2 mm/yr and 1.0–1.5 mm/yr rates of falling isotherms in hanging wall and footwall, respectively, error in the timing of closure events are 0.5–1.0 Myr and 0.067–0.1 Myr, respectively, per 100 m of error in vertical position of the sample. Thus, even if our approach of using the median depth of the samples is in error by several hundred meters, the age error introduced to the closure event is small compared to the standard error in the mean age for the mineral system. We estimate a nominal age error in the model closure event curves to be the standard error in the radiometric age of the main systems, or about ±10% of the measured age. For the hanging wall this is (0.1)(50 Ma) = ± 5 Myr, and for the footwall (0.1)(25 Ma) = ± 2.5 Myr.

According to this approach, Figure 14 shows our estimates of the time of closure events for each mineral system, as a function of structural-*Z* in both the hanging wall and footwall. In general, closure events at $Z = 0$ are, within error, the same for AFT, at about 10 to 20 Ma, but differ markedly for all higher temperature systems. The models are very similar for Profiles 1 through 4, with the exception of pre-Alpine (>60 Ma) ZFT ages in the footwall on Profile 1. The abrupt younging of the ZFT ages moving from Profile 1 to Profile 2 appears to "capture" the presence of the ZFT closure isotherm (240°C) in the footwall at ~25 Ma, because there is no (known) major structural break in the footwall between these two profiles.

Profile 5 is distinctive in having younger hanging wall ZHe and ZFT ages than Profiles 1 through 4. There are important differences between the Pennine, Margna complex, and Austroalpine structural levels along Profile 5. As originally noted by Bachmann et al. (2009), there are a series of anomalously young mica Rb/Sr ages (circa 50 Ma) located along the top of the Margna complex (blue triangles in Figure 4) that appear to record the onset of Tertiary Alpine deformation and metamorphism. We corroborated this result with a Tertiary $^{40}Ar/^{39}Ar$ white mica age (50.0 ± 0.6 Ma) from an S-C mylonite near the top of the Margna complex in the Corvatsch digitation (at the summit of Piz Corvatsch). These early Tertiary ages contrast with Paleozoic Ar/Ar mica ages that occur a few hundred meters structurally above the mylonite in the lower Bernina nappe at Fuorcla da la Sella, and hence, we refer to this contact between the Margna complex with its Corvatsch digitation and the Lower East Alpine Bernina nappe as the Corvatch detachment fault (CDF on Figures 10 and 14, Profile 5) that was active during the Eocene and possibly later. The Margna complex forms a unique cooling curve (pink boxes, Figure 15) that indicates rapid cooling from middle to lowest greenschist facies by the early Tertiary followed by a "stewing" and/or slow-cooling period until near the end of the Oligocene at which time it reaches ZHe closure temperature. This general pattern of rapid cooling followed by an isothermal "stewing" is very similar to that recorded in the Sesia-Lanzo zone in the Western Alps (cf. Figure 9 in Hurford et al., 1989).

We use the vertical age gradients (Figure 14) to estimate the mean age of a closure event for each system at $Z = 0$ to construct a composite cooling history for the central parts of the hanging wall, footwall, and Margna complex (Figure 15 and Table 3). We average the age estimates for cooling events in Profiles 2, 3, and 4, which are very similar, but treat Profiles 1 and 5 as separate entities. The thermal history allows us to make an estimate of the two parameters defined in section 1: the time of thermal equilibration of the hanging wall and footwall, t_e, and the difference in temperature between hanging wall and footwall at a given time during Pennine metamorphism, ΔT. If we have interpreted the thermal history correctly, the temperature contrast between hanging wall and footwall at 40 Ma, ΔT_{40}, was approximately 170°C, when the difference in depth between the Pennine and Austroalpine realms may have been ~1.0 GPa (~30 km depth) (Figure 15b).

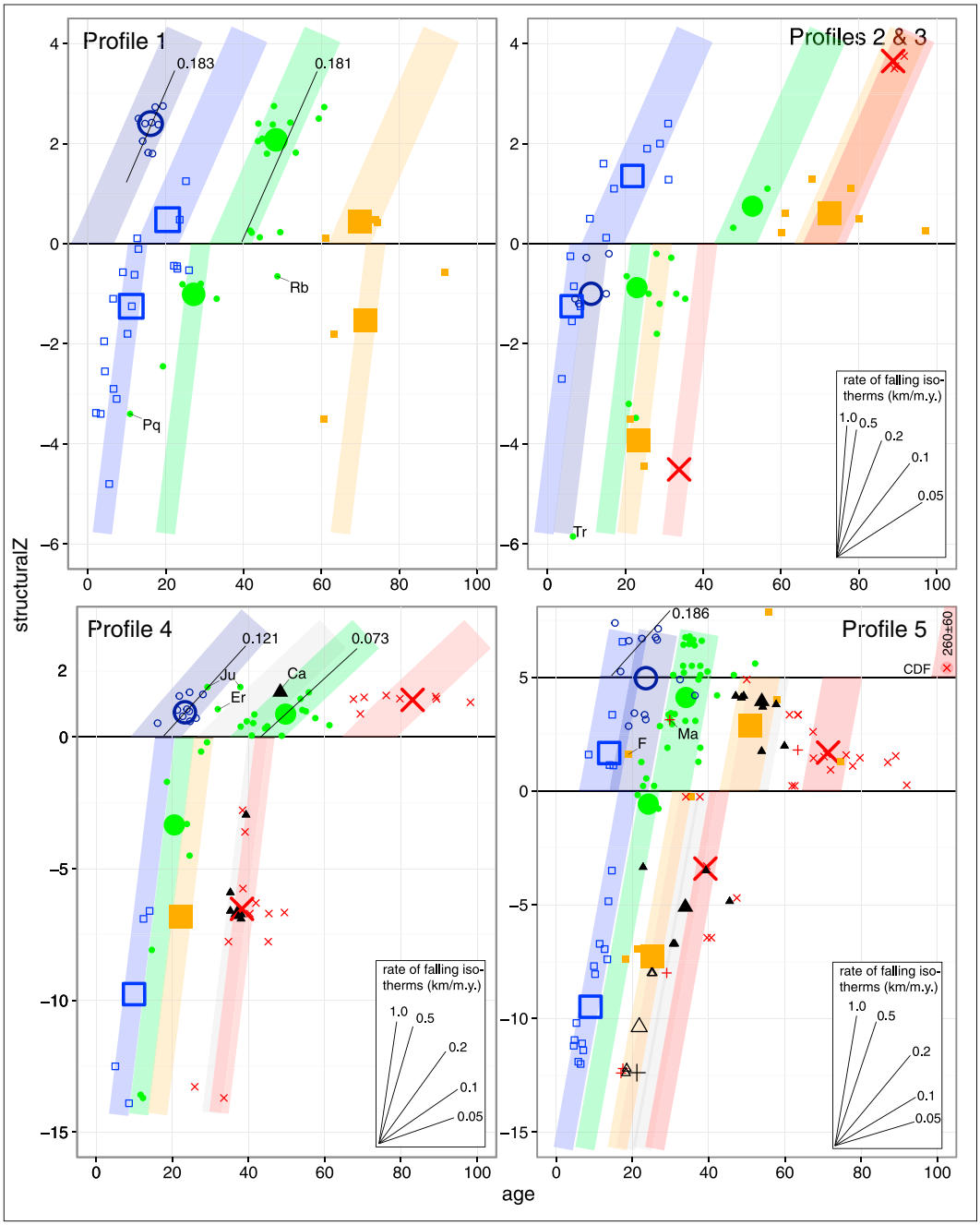

Figure 14. Structural-*Z* versus age models from the five profiles defined in this study, based on raw data shown in Figures 4, 7, 8, and 10. Colored swaths have been assigned cooling slopes that approximate what is observed by either formal regression of raw data points (e.g., hanging wall curves in Figure 9) or by a smoothed best fit region, guided by sufficient density of data points on certain profiles (e.g., ZHe and KArWM in Profile 4, AFT in Profiles 1 and 5) and existing models of cooling rates (e.g., Evans, 2011; Hurford et al., 1989). Swath color follows Figure 10. The slope of each swath is projected to the $Z = 0$ structural datum. Large summary points for each system are plotted according to mean age and median structural-*Z* as in Figure 10, and shaded swaths are projected from these points. Width of swaths represent a 10% error on the nominal measured age in hanging wall (5 Myr) and footwall (2.5 Myr) and are not intended to capture every data point. Outlier abbreviations follow Figure 10. Note that scale of structural-*Z* is the same in the top two plots but varies in the bottom two plots.

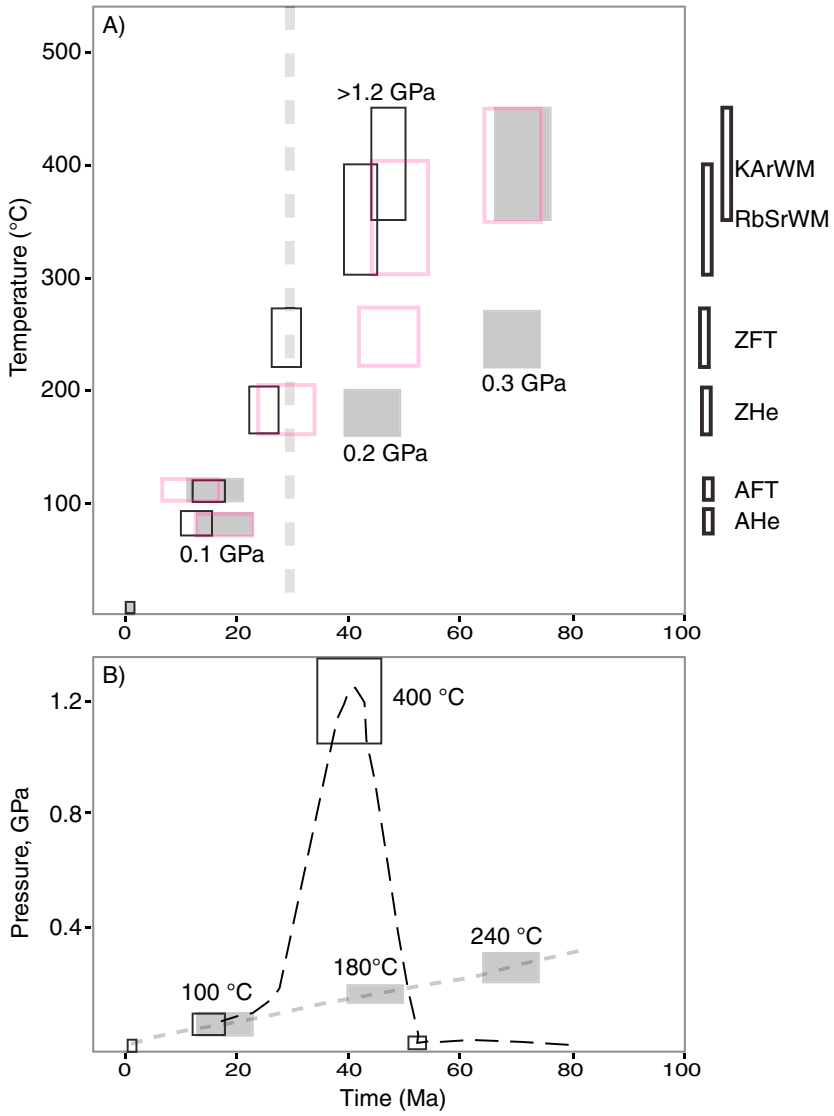

Figure 15. (a) Temperature versus time cooling paths and (b) pressure versus time paths derived from our thermal models for the Austroalpine hanging wall (closed gray boxes) and Pennine footwall (open black boxes) based on average and projected data shown in Figure 14 and Table 3. The Margna complex (pink rectangles) departs from the rest of the Austroalpine hanging wall at circa 50 Ma and joins the footwall at circa 25 Ma. Vertical dashed line is approximate age of Bergell intrusion. Vertical rectangles on the side of the plot show the range of likely closure temperatures for each of the indicated systems. This range is what determines the vertical extent of the boxes representing the tectonic units.

According to our model, t_e occurs somewhere between 29 and 18 Ma. The juxtaposition of Austroalpine and Pennine domains is traditionally regarded as having occurred prior to the intrusion of the Bergell pluton at 32–30 Ma (Nievergelt et al., 1996; Schmid et al., 1996). However, the footwall did not pass through 240°C (Tc for ZFT) until circa 29 Ma at the earliest, whereas the hanging wall was already residing below the Tc for ZHe for approximately 15 Myr prior to this time (Figures 11, 14, and 15, and Table 3). Even at 30 Ma, our cooling curves demonstrate that the hanging wall and footwall had not yet thermally equilibrated, and their temperature difference, ΔT_{30}, was still ~90°C, greater than the difference between ZFT and ZHe closure (~60°C). We note that our samples come from outcrops that are too distant from the Bergell intrusion for the closure systematics to have been perturbed by its thermal aureole or any form of contact metamorphism.

AHe and AFT fission track ages are somewhat complex and locally inverted with AHe ages being slightly older, as has been observed before in these two systems (e.g., Flowers & Kelley, 2011). Age intercepts at

Table 3
Ages Used to Make the T-t Plot in Figure 15 Determined by Projecting Age Gradients in Figure 14 to the Intercept at Z = 0

Profile	AHe	AFT	ZHe	ZFT	RbSrWM	KArWM
Hanging wall						
1	3	18	37	68	-	-
2,3	-	14	45	69	-	72
4	18	-	43	-	35	72
5	18	12	29	47	49	69
Footwall						
	AHe	AFT	ZHe	ZFT	RbSrWM	KArWM
1	-	13	29	74	-	-
2,3	13	8	24	30	-	-
4	-	18	23	28	42	47
5	-	19	25	33	43	43

Note. Uncertainty on the ages is assigned to be 10% of the nominal cooling age, that is, 5 Myr for the hanging wall and 2.5 Myr for the footwall.

Z = 0 for the AFT and AHe transects from Profiles 2, 3, and 4 are roughly the same: 18, 13, and 8 Ma in the footwall versus 18 and 14 Ma in the hanging wall (Table 3), which indicates that thermal equilibration occurred by the time the two domains reached AFT and/or AHe closure. Thus, our thermal model allows the lower bound on the timing of footwall and hanging wall thermal equilibration, t_e, to be as young as 18 Ma (ΔT_{18} = 0°C). Even so, we favor thermal equilibration to have occurred closer to 29 Ma to perhaps as young as 24 Ma, i.e., middle to late Oligocene time.

4.2. Palinspastic Implications

The sharp discontinuities in both age and age gradients (Figure 11), and the contrasting thermal histories of the hanging wall and footwall (Figure 14), cannot be maintained in situ for any significant length of geologic time and require wholesale late emplacement of the Penninic mass, with final juxtaposition after 29 Ma. Markedly contrasting age patterns are typical of Cordilleran metamophic core complexes and other large normal fault systems and are generally interpreted to indicate a magnitude of displacement that is at least the width of structural overlap between hanging wall and footwall (e.g., Singleton et al., 2014; Stöckli, 2005). For the Austroalpine-Pennine transition, the structural overlap between masses with contrasting thermal histories is about 70 km from north to south (Figures 4 and 13), indicating that the northward component of Penninic motion relative to the Austroalpine allochthon is at least this large, in good agreement with Weh's (1998) structurally derived estimate of 68 km. Although the net motion probably also has a large (but unknown) eastward component, the overall motion appears to be at a high angle to the overall ENE-WSW trend of the Alps at this longitude. It is therefore kinematically distinct from, and earlier than, Miocene orogen-parallel extension that is well known from the Western and Eastern Alps (e.g., Campani et al., 2010; Favaro et al., 2017; Selverstone, 2005).

A survey of published cross-sectional reconstructions for the Alps, particularly through the easternmost part of the Pennine zone (755,000 easting; e.g., Schmid et al., 1996), indicates very little enthusiasm among most authors for large amounts of top-south motion of the Austroalpine allochthon relative to the Pennine zone. For these models, where possible, we compiled the relative north-south position of key material points in the Pennine zone relative to a fixed point "A" within the Austroalpine allochthon through time (Figure 16). Material points include what are now the lobate northern "noses" of the three highest crystalline nappes (Adula, Tambo, and Suretta, e.g., Figure 16, inset). Two of the models are reconstructions of cross sections spanning the entire orogen (Schmid et al., 1996; Froitzheim et al., 2008; Figure 16a). Three are based on more local, nappe-scale, reconstructions (i.e., Suretta, Scheiber et al., 2012; Gotthard-Adula, Wiederkehr et al., 2009; and Grava, Weh, 1998; Figure 16b). Two are based on models using numerical (Gerya et al., 2002) and experimental (Boutelier et al., 2004) techniques (Figure 16c). Of the five geologically based models, two present little to no southward motion of the Austroalpine allochthon relative to the upper Pennine nappes, two indicate ~20 km of top-south motion between 40 and 30 Ma, and one presents approximately 70 km of top-south motion between 40 and 20 Ma. In comparison, the numerical model predicts ~40 km of top-south motion, and the experimental model features nearly 100 km top-south motion.

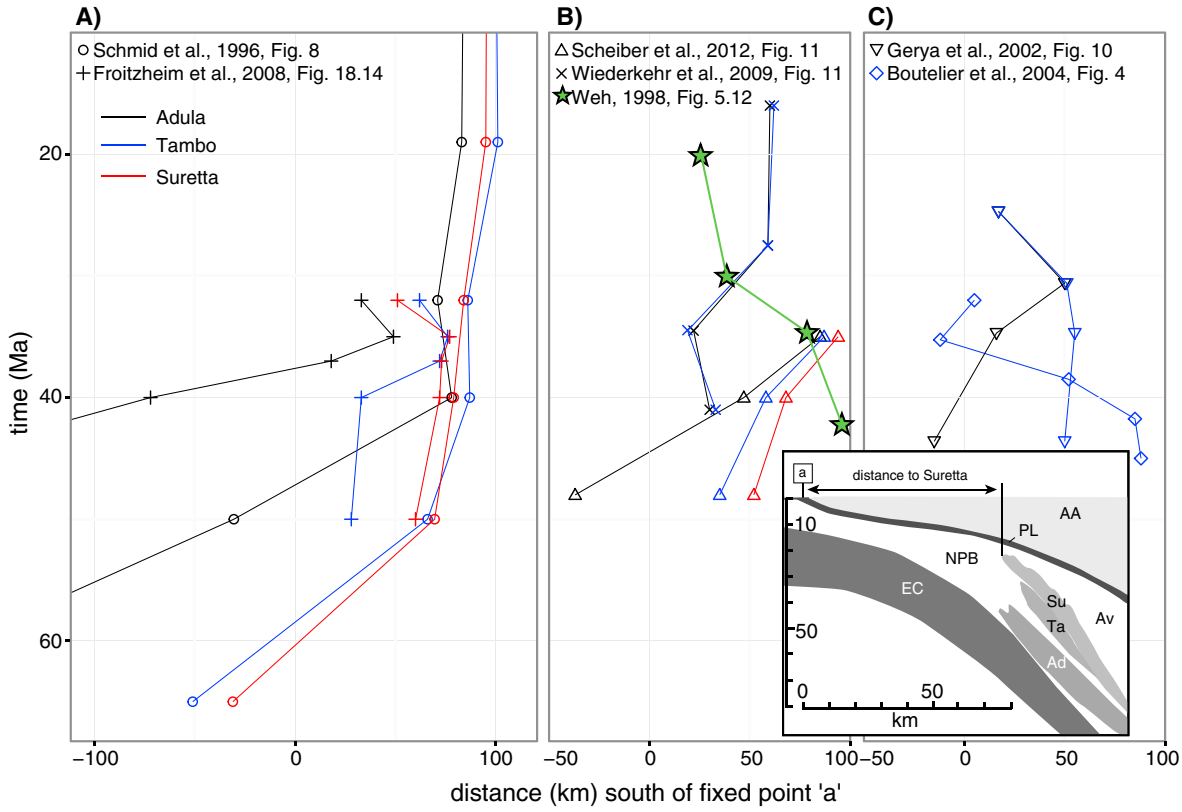

Figure 16. North-south motion of material points in the Alpine accretionary wedge relative to a fixed point in the Austroalpine allochthon (i.e., Austroalpine overlap distance), measured from the front (north end) of the Austroalpine allochthon to the front (north end) of the nappe in question (see inset for example). Plot is organized by (a) regional reconstructions, (b) local nappe-scale reconstructions, and (c) numerical and analog modeling. Inset profile from Schmid et al. (1996). AA: Austroalpine allochthon, Ad: Adula, Av: Avers Bündnerschiefer, EC: European crust, NPB: North Penninic Bündnerschiefer, PL: Platta, Su: Suretta, and Ta: Tambo.

A simple palinspastic reconstruction, based on our models of the low-temperature cooling histories, places the Penninic footwall in a subduction channel just south of the present-day Insubric fault, with an upper end at a paleodepth of 10 km (approximate thickness of the orogenic lid) at 29 Ma, just after intrusion of the Bergell complex (Figure 17). For a nominal inclination of the channel of 45° (a modest angle compared to modern Mediterranean Benioff zones), the lower end of the Penninic mass (southern part of the Adula nappe) would have lain at a paleodepth of at least 10 + 80/(cos 45) = 74 km, corresponding to a pressure of about 2.2 GPa, which is within the observed range of 2.0–3.0 GPa estimates for (U)HP metamorphism at circa 32–34 Ma in the Monte Duria area (Hermann et al., 2006; Herwartz et al., 2011; Meyre et al., 1999). Assuming this geometric analysis is basically correct, it provides independent confirmation that pressures recorded by (U)HP metamophic assemblages reflect paleodepth, rather than zones of localized "tectonic overpressure" (e.g., Mancktelow, 1993, 1995; Pleuger & Podladchikov, 2014; Schenker et al., 2015). In further support of this analysis, in the most southern, deepest exposed levels of the Pennine zone, near exposures of UHP eclogites at Cima Lunga and Alpe Arami, detailed zircon geochronology and geochemistry of Alpine migmatites indicate that syntectonic partial melting and crystallization of metasedimentary and metaigneous rocks occurred over a protracted period, under isothermal conditions of 620 to 700°C, from 31 Ma to 22 Ma (Rubatto et al., 2009). This is almost precisely the interval in which we propose emplacement of shallower portions of the Pennine zone against the base of the Austroalpine allochthon, indicating that deeper portions of the system were tectonically and magmatically active during Pennine unroofing at shallower levels.

Given that the Austroalpine allochthon lay above the Pennine zone during mid-Tertiary exhumation (Figure 17), the steep, closely spaced age-depth curves in the footwall (Figures 10 and 14) cannot be the result of rapid erosion, at least within the study area outlined in Figure 4. Rather, they record rapid cooling in the wake of fault juxtaposition of the subduction channel assemblage against shallow upper crustal rocks in the forearc wedge, which had a thickness of $<$10 km by that time (Figures 15 and 17).

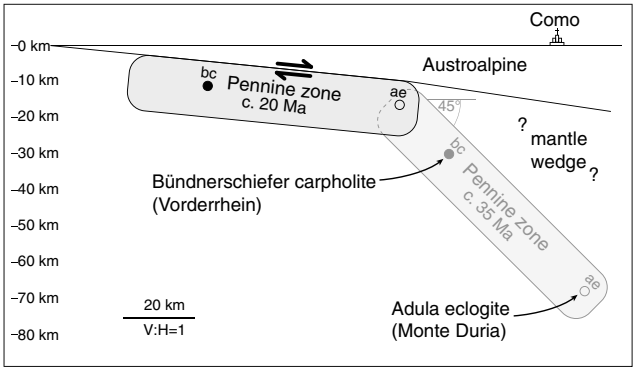

Figure 17. Schematic north-south reconstruction of the Central Alps at circa 35 and 20 Ma which emphasizes that the high-P metamorphic grade of rocks in the Pennine zone can be accounted for by subducting a coherent slab approximately 80 km in length by 15 km thick to 10 to 80 km depth. Sketch also emphasizes the distance (>60 km) the exhuming Pennine zone had to travel in circa 10 Myr to become juxtaposed against the thin overriding Austroalpine plate resulting in a complete mismatch of rocks between hanging wall and footwall along the entire length of the Austroalpine "overthrust."

From a methodological perspective, we stress the fact that without the use of the two zircon thermochronometric systems (Figure 15), the primary contrasts and estimates of the timing of key tectonic events are difficult to recover in upper crustal exposures of accretionary systems where temperatures of deformation are <300°C. In this case, to rely solely on AFT, AHe, and Ar/Ar systematics in micas, the null hypothesis that the hanging wall and footwall had identical thermal histories between circa 40 Ma and the present could not be falsified (Figure 15).

4.3. On the Steady State Theory of the Alps

In the past two decades, there have been numerous attempts to use thermochronometric systems to determine uplift and exhumation rates across the Alps (e.g., Bernet et al., 2001, 2004, 2009; Fox et al., 2016; Hurford, 1986; Hurford et al., 1989), the accuracy of which depends upon the initial assumption that the Alps have behaved (mostly) as a steady state, erosionally dominated, tectonically inert system since at least middle Miocene, circa 15 Ma (Bernet et al., 2001, 2004) to possibly early Oligocene time, circa 30 Ma (Fox et al., 2016), the latter time limit determined approximately by the intrusion age of the Bergell pluton. In order to model steady state behavior, some representative or "a priori" exhumation rate must be applied and modulated across the entire orogen without regard for any bounding structures that may control exhumation rate. To the extent that the models (e.g., Fig. 6 in Fox et al., 2016) go far enough back in time to overlap with the differential unroofing rates of the Pennine and Austroalpine domains in eastern Switzerland, they are not an accurate description of Alpine unroofing.

Despite the flawed initial assumption of steady state behavior for the Alps in pre-Miocene time, at least two conclusions drawn from these studies support our conclusions: (1) Bernet et al. (2004) present peak ages for detrital ZFT populations that support the model of Pennine zone exhumation that we present here. In particular, for every major drainage on the southern end of the orogen there is a ZFT population (i.e., the P3 peak-fit population ages in Table 1 of Bernet et al., 2004) that falls in the range 24 to 36 Ma, indicating that Pennine zone cooling through 240°C occurred from late Eocene well into the Oligocene. Given that detrital rocks represent nonspecific sampling over a wide catchment area, these detrital ZFT ages agree rather well with the bedrock data compilation presented here. (2) Fox et al. (2016) conclude that there was a "major reorganization" of the Alpine orogen at 20 Ma. This is consistent with our prediction that Pennine zone thermal equilibration could have occurred as late as circa 18 Ma. Thus, we posit that this "major reorganization" occurred at the end of the emplacement of the Penninic wedge. Importantly, the Alps were not in any kind of steady state until after this period of reorganization.

5. Conclusions

The mismatch in Tertiary thermal histories between the Austroalpine allochthon and its Penninic substrate across the strike of the Central Alps (Figure 14) indicates that no point currently exposed in the footwall had been emplaced against the hanging wall until some time between 29 and 18 Ma. Given that the strata within the Grava nappe in the northern half-window experienced peak metamorphic pressures of order 1.0–1.2 GPa, and the Austroalpine allochthon was already at temperatures of ≤180°C at the same time (circa 35 Ma), top-south to top-southeast normal fault motion of at least 60 km along the base of the Austroalpine allochthon is required to juxtapose the two rock masses. Our data strongly support the kinematic analysis of Weh (1998) and at least the kinematic consequences of the models of Gerya et al. (2002) and Boutelier et al. (2004). We note that even if the displacement rate on the fault system were 1 to 2 cm/yr, it would still take at least 3 to 6 Myr to accommodate the 60 km of minimum motion. At a rate of 1 cm/yr with 100 km of displacement, the duration of motion may have been in the 10 Myr range, likely beginning with the youngest estimates of (U)HP metamorphism at Monte Duria (circa 33 Ma) and ending some time between 29 and 18 Ma. We note also that the timing of motion during this interval agrees well with the timing of thermal equilibration between hanging wall and footwall in the Tauern Window, which

occurred between circa 25 and 15 Ma (Luth & Willingshofer, 2008). We also note that, although the thermal structure of the subduction channel is complex, the north-south age gradients in the ZFT and ZHe systems, as noted in Figures 7c and 7d, are of order 1 cm/yr. To the extent that this gradient reflects passage of the wedge through a closure isotherm at constant depth, it implies a duration of approximately 7 Myr to accommodate 70 km of relative motion.

Much or all of the normal motion occurred during two key events in Alpine evolution. The first is at the onset of foredeep sedimentation on both Europe and Adria at about 32 Ma (Lower Marine Molasse on Europe, Villa Olmo conglomerate on Adria), with most subsidence occurring between 30 and 15 Ma. The second is major horizontal shortening of the European passive margin that formed the Helvetic nappes (e.g., Trümpy, 1980). In regard to the latter, the most rapid period of flysch deposition in the Helvetic foredeep occurred in latest Eocene to early Oligocene time (34-30 Ma), and estimates of the timing of the various phases of thrust and nappe formation range from early Oligocene to early Miocene time (30-15 Ma). The formation of the Helvetic nappes thus may have been coeval with final juxtaposition of the Austroalpine and Penninic domains, rather than postdating it as has been commonly assumed. If so, the Oligocene to early Miocene collisional history of the Alps would represent an analogy to the Miocene phase of collision in the Himalaya, when the South Tibetan detachment system and the Main Central thrust simultaneously accommodated large-magnitude normal and thrust motion, respectively (e.g., Burchfiel et al., 1992). Recent studies suggest that the two systems may have only been simultaneously active in brief, sporadic phases of a few million years (e.g., Carosi et al., 2013; Chambers et al., 2011; Kellett et al., 2013; Montomoli et al., 2017), which are somewhat brief in comparison to the maximum of circa 11 Ma we suggest for the duration of activity on the Pennine-Austroalpine contact zone in eastern Switzerland. The truncation of the Turba zone by the 30 Ma Bergell intrusion may provide a similar constraint to the Himalayan studies, suggesting that the Turba zone may have been active only during the earliest few million years of exhumation, after which time activity was likely accommodated on nearby structures above or below it, such as the Corvatsch detachment fault or the Forcola normal fault, respectively.

In regard to the development of the peri-Alpine foredeep basins, the interposition of a 15–20 km-thick mass of subduction complex material between the thin upper crustal "flake" of the Austroalpine allochthon and the southern margin of Europe would have represented a major crustal thickening event. This was likely the first time at which crustal thickness anywhere in the system exceeded 30 to 35 km, driving range-scale redistribution of crustal mass via rapid subaerial erosion of the newly forming mountain belt. If we measure the collision of Adria and Europe by, for example, the position of the Adula nappe (Monte Duria) relative to the Austroalpine allochthon, then collision was well underway by circa 40 Ma, as generally depicted in cross-sectional models of the Alps (e.g., Schmid et al., 2004). Importantly, if the emplacement of a combined Pennine-Helvetic mass occurred mainly between 30 and 20 Ma, along with development of the foredeep basins, then mountain building in the Alps is not so much a result of continent-continent collision as it is the result of an episode of buoyant return flow and concentrated accumulation of subduction channel material near the top of the channel (e.g., Butler et al., 2013; Chemenda et al., 1995). The relatively late (post-Bergell intrusive) timing of a culminating phase of unroofing via such return flow is generally consistent with a slab-breakoff event in the interval 35–30 Ma as a "trigger" (Froitzheim et al., 2008; von Blanckenburg & Davies, 1995), but implies a 5–10 Ma delay between cause and effect.

Acknowledgments
New data presented here are available through the EarthChem database: DOI: 10.1594/IEDA/100727 (Price et al., 2017). We thank Becky Flowers and Jim Metcalf at the CU TRaIL facility for providing ZHe analyses; Ray and Margaret Donelick at A to Z, Inc. for providing ZFT analyses; Mark Garcia, Janet Harvey, Nathan Niemi, Sarah Bala, and Renee Pillers for help with mineral separations; Lindsey Hedges for sharing her considerable experience in the laboratory; and Bryan Palmintier, Lukas Flükiger Nibourel, Luca Malatesta, Kari Price, Peter Nievergelt, and Dominik Letsch for help in the field and with navigating Switzerland (white gas = reinbenzin, available at the Apotheke). Funding for this work was supported by the NSF Tectonics program, through award EAR 14-51055 to Brian Wernicke. The manuscript was considerably improved by comments from Clare Bond, USGS external reviewer Bill Rehrig, Guest Associate Editor Rodolfo Carosi, and an anonymous reviewer. Any use of trade, product, or firm names is for descriptive purposes only and does not imply endorsement by the U.S. Government.

References

Allen, P. A., & Allen, J. R. (2006). *Basin analysis: Principles and application to petroleum play assessment* (3rd ed., p. 451). Oxford, UK: Wiley-Blackwell.

Angiboust, S., Agard, P., Raimbourg, H., Yamato, P., & Huet, B. (2011). Subduction interface processes recorded by eclogite facies shear zones (Monviso, W. Alps). *Lithos*, *127*, 222–238. https://doi.org/10.1016/j.lithos.2011.09.004

Angiboust, S., Glodny, J., Oncken, O., & Chopin, C. (2014). In search of transient subduction interfaces in the Dent Blanche-Sesia tectonic system (W. Alps). *Lithos*, *205*, 298–321. https://doi.org/10.1016/j.lithos.2014.07.001

Argand, É. (1916). Sur l'arc des Alpes Occidentales. *Eclogae Geologicae Helvetiae*, *14*, 145–191.

Armstrong, R. L., Jäger, E., & Eberhardt, P. (1966). A comparison of K-Ar and Rb-Sr ages on Alpine biotites. *Earth and Planetary Science Letters*, *1*, 13–19.

Augenstein, C. (2012). The formation of the Lepontine Dome, unpublished PhD thesis, Australian National University, 357 p.

Axen, G. J., Bartley, J. M., & Selverstone, J. (1995). Structural expression of a rolling hinge in the footwall of the Brenner Line normal fault, Eastern Alps. *Tectonics*, *14*, 1380–1392. https://doi.org/10.1029/95TC02406

Bachmann, R., Glodny, J., Oncken, O., & Seifert, W. (2009). Abandonment of the South Penninic–Austroalpine palaeosubduction zone, Central Alps, and shift from subduction erosion to accretion: Constraints from Rb/Sr geochronology. *Journal of the Geological Society*, *166*, 217–231.

Beaumont, C., Jamieson, R. A., Butler, J. P., & Warren, C. J. (2009). Crustal structure: A key constraint on the mechanism of ultra-high-pressure rock exhumation. *Earth and Planetary Science Letters*, *287*, 116–129. https://doi.org/10.1016/j.epsl.2009.08.001

Beltrando, M., Lister, G. S., Rosenbaum, G., Richards, S., & Forster, M. A. (2010). Recognizing episodic lithospheric thinning along a convergent plate margin: The example of the early Oligocene Alps. *Earth-Science Reviews*, *103*, 81–98. https://doi.org/10.1016/j.earscirev.2010.09.001

Bernet, M., Brandon, M., Garver, J., Balestieri, M. L., Ventura, B., & Zattin, M. (2009). Exhuming the Alps through time: Clues from detrital zircon fission-track thermochronology. *Basin Research*, *21*(6), 781–798. https://doi.org/10.1111/j.1365-2117.2009.00400.x

Bernet, M., Brandon, M. T., Garver, J. I., & Molitor, B. R. (2004). Fundamentals of detrital zircon fission-track analysis for provenance and exhumation studies with examples from the European Alps. *Geological Society of America Special Papers*, *378*, 25–36.

Bernet, M., Zattin, M., Garver, J. I., Brandon, M. T., & Vance, J. A. (2001). Steady-state exhumation of the European Alps. *Geology*, *29*, 35–38.

Boutelier, D., Chemenda, A., & Jorand, C. (2004). Continental subduction and exhumation of high-pressure rocks: Insights from thermo-mechanical laboratory modeling. *Earth and Planetary Science Letters*, *222*, 209–216.

Burchfiel, B. C., & Royden, L. H. (1985). North–south extension within the convergent Himalayan region. *Geology*, *13*, 679–682.

Burchfiel, B. C., Zhiliang, C., Hodges, K. V., Yuping, L., Royden, L. H., Changrong, D., & Jiene, X. (1992). The South Tibetan detachment system, Himalayan orogen: Extension contemporaneous with and parallel to shortening in a collisional mountain belt. *Geological Society of America Special Papers*, *269*, 1–41.

Burg, J. P., & Gerya, T. V. (2005). The role of viscous heating in Barrovian metamorphism of collisional orogens: Thermomechanical models and application to the Lepontine Dome in the Central Alps. *Journal of Metamorphic Geology*, *23*, 75–95.

Butler, J. P., Beaumont, C., & Jamieson, R. A. (2013). The Alps 1: A working geodynamic model for burial and exhumation of (ultra)high-pressure rocks in alpine-type orogens. *Earth and Planetary Science Letters*, *377–378*, 114–131. https://doi.org/10.1016/j.epsl.2013.06.039

Butler, J. P., Beaumont, C., & Jamieson, R. A. (2014). The Alps 2: Controls on crustal subduction and (ultra)high-pressure rock exhumation in Alpine-type orogens. *Journal of Geophysical Research: Solid Earth*, *119*, 5987–6022. https://doi.org/10.1002/2013JB010799

Campani, M., Mancktelow, N., Seward, D., Rolland, Y., Muller, W., & Guerra, I. (2010). Geochronological evidence for continuous exhumation through the ductile-brittle transition along a crustal scale low-angle normal fault: Simplon fault zone, Central Alps. *Tectonics*, *29*, TC3002. https://doi.org/10.1029/2009TC002582

Carosi, R., Montomoli, C., Rubatto, D., & Visonà, D. (2013). Leucogranite intruding the South Tibetan Detachment in western Nepal: Implications for exhumation models in the Himalayas. *Terra Nova*, *25*, 478–489.

Chambers, J., Parrish, R., Argles, T., Harris, N., & Horstwood, M. (2011). A short-duration pulse of ductile normal shear on the outer South Tibetan detachment in Bhutan: Alternating channel flow and critical taper mechanics of the eastern Himalaya. *Tectonics*, *30*, TC2005. https://doi.org/10.1029/2010TC002784

Challandes, N., Marquer, D., & Villa, I. M. (2003). Dating the evolution of C–S microstructures: a combined $^{40}Ar/^{39}Ar$ step-heating and UV laserprobe analysis of the Alpine Roffna shear zone. *Chemical Geology*, *197*, 3–19.

Chemenda, A. I., Mattauer, M., Malavieille, J., & Bokun, A. N. (1995). A mechanism for syn-collisional rock exhumation and associated normal faulting: Results from physical modeling. *Earth and Planetary Science Letters*, *132*, 225–232.

Chopin, C. (2003). Ultrahigh-pressure metamorphism: Tracing continental crust into the mantle. *Earth and Planetary Science Letters*, *212*, 1–14. https://doi.org/10.1016/S0012-821X(03)00261-9

Ciancaleoni, L. (2005). Deformation processes during the last stages of the continental collision: The brittle-ductile fault systems in the Bergell and Insubric areas (Eastern Central Alps, Switzerland–Italy). Unpublished PhD dissertation, University of Neuchâtel, Switzerland, 202 p.

Ciancaleoni, L., & Marquer, D. (2008). Late Oligocene to early Miocene lateral extrusion at the eastern border of the Lepontine Dome of the Central Alps (Bergell and Insubric areas, eastern Central Alps). *Tectonics*, *27*, TC4008. https://doi.org/10.1029/2007TC002196

Dalrymple, G. B., Alexander, E. C., Lanphere, M. A., & Kraker, G. P. (1981). Irradiation of samples for $^{40}Ar/^{39}Ar$ dating using the geological survey TRIGA reactor. USGS Professional Paper 1176. U.S. Geological Survey, Reston, VA, United States. 54 p. https://pubs.usgs.gov/pp/1176/report.pdf

Dewey, J. F. (1988). Extensional collapse of orogens. *Tectonics*, *7*, 1123–1139.

Donelick, R. A., O'Sullivan, P. B., & Ketcham, R. A. (2005). Apatite fission track analysis. *Reviews in Mineralogy and Geochemistry*, *58*, 49–94.

Engi, M., Bousquet, R., & Berger, A. (2004). Central Alps. *Mitteilungen der Oesterreichischen Mineralogischen Gesellschaft*, *149*, 157–173.

Ernst, W. G. (1975). Systematics of large-scale tectonics and age progressions in Alpine and Circum-Pacific blueschist belts. *Tectonophysics*, *26*, 229–246.

Ernst, W. G. (2005). Alpine and Pacific styles of Phanerozoic mountain building: Subduction-zone petrogenesis of continental crust. *Terra Nova*, *17*, 165–188.

Evans, S. (2011). Timing of exhumation of the eastern Central Alps from zircon and apatite (U-Th)/He thermochronology (Graubünden, Switzerland), Unpublished M.S. thesis, University of Kansas, 226 p. Retrieved from https://kuscholarworks.ku.edu/bitstream/handle/1808/9746/Evans_ku_0099M_11901_DATA_1.pdf?sequence%20=%201%26amp%3BisAllowed%20=%20y

Farley, K. (2002). (U-Th)/He Dating: Techniques, Calibrations, and Applications. *Reviews in Mineralogy and Geochemistry*, *47*, 819–844.

Favaro, S., Handy, M. R., Scharf, A., & Schuster, R. (2017). Changing patterns of exhumation and denudation in front of an advancing crustal indenter, Tauern Window (Eastern Alps). *Tectonics*, *36*, 1053–1071. https://doi.org/10.1002/2016TC004448

Fitzgerald, P. G., Duebendorfer, E. M., Faulds, J. E., & O'Sullivan, P. (2009). South Virgin–White Hills detachment fault system of SE Nevada and NW Arizona: Applying apatite fission track thermochronology to constrain the tectonic evolution of a major continental detachment fault. *Tectonics*, *28*, TC2001. https://doi.org/10.1029/2007TC002194

Fitzgerald, P. G., Fryxell, J. E., & Wernicke, B. P. (1991). Miocene crustal extension and uplift in southeastern Nevada: Constraints from fission track analysis. *Geology*, *19*, 1013–1016. https://doi.org/10.1130/0091-7613(1991)019<1013:MCEAUI>2.3.CO;2

Flisch, M. (1986). Die Hebungsgeschichte der oberostalpinen Silvretta-Decke seit der mittleren Kreide. *Bulletin der Vereinigung Schweiz Petroleum-Geologen und -Ingenieure*, *53*, 23–49.

Flowers, R. M., & Kelley, S. A. (2011). Interpreting data dispersion and "inverted" dates in apatite (U-Th)/He and fission-track datasets: An example from the U.S. midcontinent. *Geochimica et Cosmochimica Acta*, *75*, 5169–5186.

Fox, M., Herman, F., Willett, S. D., & Schmid, S. M. (2016). The exhumation history of the European Alps inferred from linear inversion of thermochronometric data. *American Journal of Science*, *316*, 505–541.

Froitzheim, N., Plašienka, D., & Schuster, R. (2008). Alpine tectonics of the Alps and Western Carpathians. In T. McCann (Ed.), *The geology of Central Europe, volume 2, Mesozoic and Cenozoic* (pp. 1141–1232). London: Geological Society.

Froitzheim, N., Pleuger, J., & Nagel, T. J. (2006). Extraction faults. *Journal of Structural Geology*, *28*, 1388–1395.

Froitzheim, N., Schmid, S. M., & Conti, P. (1994). Repeated change from crustal shortening to orogen-parallel extension in the Austroalpine units of Graubunden. *Eclogae Geologicae Helvetiae*, *87*, 559–612.

Froitzheim, N., Schmid, S. M., & Frey, M. (1996). Mesozoic paleogeography and the timing of eclogite-facies metamorphism in the Alps: A working hypothesis. *Eclogae Geologicae Helvetiae*, *89*, 81–110.
Gerya, T. V., Stöckhert, B., & Perchuk, A. L. (2002). Exhumation of high-pressure metamorphic rocks in a subduction channel: A numerical simulation. *Tectonics*, *21*, TC1056. https://doi.org/10.1029/2002TC001406
Handy, M. R., Herwegh, M., Kamber, B. S., Tietz, R., & Villa, I. M. (1996). Geochronologic, petrologic and kinematic constraints on the evolution of the Err-Platta boundary, part of a fossil continent-ocean suture in the Alps (eastern Switzerland). *Schweizerische Mineralogische und Petrographische Mitteilungen*, *76*, 453–474.
Hansmann, W. (1996). Age determination of the Tertiary Masino-Bregaglia (Bergell) intrusives (Italy, Switzerland): A review. *Schweizerische Mineralische und Petrographische Mitteilungen*, *76*, 421–451.
Hanson, G. N., El Tahlawi, M. R., & Weber, W. (1966). K/Ar and Rb/Sr ages of pegmatites in the south central Alps. *Earth and Planetary Science Letters*, *1*, 407–413.
Hermann, J., Rubatto, D., & Trommsdorff, V. (2006). Sub-solidus Oligocene zircon formation in garnet peridotite during fast decompression and fluid infiltration (Duria, Central Alps). *Mineralogy and Petrology*, *88*, 181–206. https://doi.org/10.1007/s00710-006-0155-3
Herwartz, D., Nagel, T. J., Münker, C., Scherer, E. E., & Froitzheim, N. (2011). Tracing two orogenic cycles in one eclogite sample by Lu-Hf garnet chronometry. *Nature Geoscience*, *4*, 178–183.
House, M. A., Wernicke, B. P., & Farley, K. A. (1998). Dating topography of the Sierra Nevada, California, using apatite (U-Th)/He ages. *Nature*, *396*, 66.
Hunziker, J. C. (1986). The evolution of illite to muscovite: An example of the behavior of isotopes in low-grade metamorphic terrains. *Chemical Geology*, *57*, 31–40.
Hunziker, J. C., Desmons, J., & Hurford, A. J. (1992). *Thirty-two years of geochronological work in the Central and Western Alps: A review of seven maps* (Vol. 13, p. 59). Switzerland: Universite de Lausanne, Institut de Geologie et Paleontologie, Lausanne.
Hunziker, J. C., Frey, M., Clauer, N., Dallmeyer, R. D., Friedrichsen, H., Flehmig, W., … Schwander, H. (1986). The evolution of illite to muscovite: Mineralogical and isotopic data from the Glarus Alps, Switzerland. *Contributions to Mineralogy and Petrology*, *92*, 157–180.
Hurford, A. J. (1986). Cooling and uplift patterns in the Lepontine Alps South Central Switzerland and an age of vertical movement on the Insubric fault line. *Contributions to Mineralogy and Petrology*, *92*, 413–427.
Hurford, A. J., Flisch, M., & Jäger, E. (1989). *Unraveling the thermo-tectonic evolution of the Alps: A contribution from fission track analysis and mica dating* (Vol. 45, pp. 369–398). Geological Society, London: Special Publications.
Inger, S., Ramsbotham, W., Cliff, R. A., & Rex, D. C. (1996). Metamorphic evolution of the Sesia-Lanzo zone, Western Alps: Time constraints from multi-system geochronology. *Contributions to Mineralogy and Petrology*, *126*, 152–168.
Jäger, E. (1962). Rb-Sr age determinations on micas and total rocks from the Alps. *Journal of Geophysical Research*, *67*, 5293–5306.
Janots, E., Engi, M., Rubatto, D., Berger, A., Gregory, C., & Rahn, M. (2009). Metamorphic rates in collisional orogeny from *in situ* allanite and monazite dating. *Geology*, *37*, 11–14.
Kellett, D. A., Grujic, D., Coutand, I., Cottle, J., & Mukul, M. (2013). The South Tibetan detachment system facilitates ultra rapid cooling of granulite-facies rocks in Sikkim Himalaya. *Tectonics*, *32*, 252–270. https://doi.org/10.1002/tect.20014
Ketcham, R. A., Gautheron, C., & Tassan-Got, L. (2011). Accounting for long alpha-particle stopping distances in (U–Th–Sm)/He geochronology: Refinement of the baseline case. *Geochimica et Cosmochimica Acta*, *75*, 7779–7791.
Knaus, A. (1990). Apatit-Spaltspurendatierungen in Rätikon (Arosazone, Östalpen). Part 1: Diploma Thesis, University of Tübingen, Germany, 60 p.
Kuiper, K. F., Deino, A., Hilgen, F. J., Krijgsman, W., Renne, P. R., & Wijbrans, J. R. (2008). Synchronizing rock clocks of Earth history. *Science*, *320*, 500–504.
Laubscher, H. P. (1983). In R. D. Hatcher, H. Williams, & I. Zeitz (Eds.), *Detachment, shear, and compression in the Central Alps* (Vol. 158, pp. 191–211). Geological Society of America Memoir. https://doi.org/10.1130/MEM158-p191
Lee, J.-Y., Marti, K., Severinghaus, J. P., Kawamura, K., Yoo, H.-S., Lee, J. B., & Kim, J. S. (2006). A redetermination of the isotopic abundances of atmospheric Ar. *Geochimica et Cosmochimica Acta*, *70*, 4507–4512.
Liati, A., Gebauer, D., & Fanning, M. (2000). U–Pb SHRIMP dating of zircon from the Novate granite (Bergell, Central Alps): Evidence for Oligocene–Miocene magmatism, Jurassic/Cretaceous continental rifting and opening of the Valais trough. *Schweizerische Mineralogische und Petrographische Mitteilungen*, *80*, 305–316.
Liniger, M. H. (1992). Der ostalpin-penninische Grenzbereich im Gebiet der nördlichen Margna-Decke (Graubünden, Schweiz), unpublished PhD dissertation, Eidgenössischen Technischen Hochschule, Zürich. 186 p.
Lister, G. S., Banga, G., & Feenstra, A. (1984). Metamorphic core complexes of Cordilleran type in the Cyclades, Aegean Sea, Greece. *Geology*, *12*, 221–225.
Luth, S. W., & Willingshofer, E. (2008). Mapping of the post-collisional cooling history of the Eastern Alps. *Swiss Journal of Geosciences*, *101*(supplement 1), S207–S223.
Mahéo, G., Gautheron, C., Leloup, P. H., Fox, M., Tassant-Got, L., & Douville, E. (2013). Neogene exhumation history of the Bergell Massif (southeast Central Alps). *Terra Nova*, *25*, 110–118. https://doi.org/10.1111/ter.12013
Mählmann, R. F. (2001). Correlation of very low grade data to calibrate a thermal maturity model in a nappe tectonic setting, a case study from the Alps. *Tectonophysics*, *334*, 1–33.
Malusà, M. G., Faccenna, C., Garzanti, E., & Polino, R. (2011). Divergence in subduction zones and exhumation of high pressure rocks (Eocene Western Alps). *Earth and Planetary Science Letters*, *310*, 21–32. https://doi.org/10.1016/j.epsl.2011.08.002
Malusà, M. G., Polino, R., Zattin, M., Bigazzi, G., Martin, S., & Piana, F. (2005). Miocene to present differential exhumation in the Western Alps: Insights from fission track thermochronology. *Tectonics*, *24*, TC3004. https://doi.org/10.1029/2004TC001782
Mancktelow, N. S. (1992). Neogene lateral extension during convergence in the Central Alps: Evidence from interrelated faulting and backfolding around the Simplonpass, Switzerland. *Tectonophysics*, *215*, 295–317.
Mancktelow, N. S. (1993). Tectonic overpressure in competent mafic layers and the development of isolated eclogites. *Journal of Metamorphic Geology*, *11*, 801–812.
Mancktelow, N. S. (1995). Nonlithostatic pressure during sediment subduction and the development and exhumation of high pressure metamorphic rocks. *Journal of Geophysical Research*, *100*(B1), 571–583.
McKenzie, D. (1972). Active tectonics of the Mediterranean region. *Geophysical Journal International*, *30*, 109–185.
McKenzie, D., & Sclater, J. G. (1971). The evolution of the Indian Ocean since the Late Cretaceous. *Geophysical Journal International*, *24*, 437–528.
Meyre, C., De Capitani, C., Zack, T., & Frey, M. (1999). Petrology of high-pressure metapelites from the Adula Nappe (Central Alps, Switzerland). *Journal of Petrology*, *40*, 199–213.

Michalski, I., & Soom, M. (1990). The Alpine thermo-tectonic evolution of the Aar and Gotthard massifs, central Switzerland: Fission track ages on zircon and apatite and K-Ar mica ages. *Schweizerische Mineralogische und Petrographische Mitteilungen*, *70*, 373–387.

Milnes, A. G., & Pfiffner, O. A. (1980). Tectonic evolution of the Central Alps in cross section St. Gallen-Como. *Eclogae Geologicae Helvetiae*, *73*, 619–633.

Milnes, A. G., & Schmutz, H. U. (1978). Structure and history of the Suretta nappe (Pennine zone, Central Alps): A field study. *Eclogae Geologicae Helvetiae*, *71*, 19–33.

Min, K., Mundil, R., Renne, P. R., & Ludwig, K. R. (2000). A test for systematic errors in $^{40}Ar/^{39}Ar$ geochronology through comparison with U/Pb analysis of a 1.1-Ga rhyolite. *Geochimica et Cosmochimica Acta*, *64*, 73–98.

Miron, G. D., Wagner, T., Walle, M., & Heinrich, C. A. (2013). Major and trace element composition and pressure–temperature evolution of rock-buffered fluids in low-grade accretionary wedge metasediments, Central Alps. *Contributions to Mineralogy and Petrology*, *165*, 981–1008. https://doi.org/10.1007/s00410-012-0844-3

Mohn, G., Manatschal, G., Beltrando, M., Masini, E., & Kusznir, N. (2012). Necking of continental crust in magma-poor rifted margins: Evidence from the fossil Alpine Tethys margins. *Tectonics*, *31*, TC1012. https://doi.org/10.1029/2011TC002961

Mohn, G., Manatschal, G., Masini, E., & Müntener, O. (2011). Rift-related inheritance in orogens: A case study from the Austroalpine nappes in Central Alps (SE-Switzerland and N-Italy). *International Journal of Earth Sciences (Geologische Rundschau)*, *100*, 937–961. https://doi.org/10.1007/s00531-010-0630-2

Mohn, G., Manatschal, G., Müntener, O., Beltrando, M., & Masini, E. (2010). Unraveling the interaction between tectonic and sedimentary processes during lithospheric thinning in the Alpine Tethys margins. *International Journal of Earth Sciences*, *99*, 75–101.

Montomoli, C., Carosi, R., Rubatto, D., Visonà, D., & Iaccarino, S. (2017). Tectonic activity along the inner margin of the South Tibetan Detachment constrained by syntectonic leucogranite emplacement in Western Bhutan. *Italian Journal of Geosciences*, *136*, 5–14.

Nänny, P. (1948). Zur geologie der Prättigauschiefer zwischen Rhättikon und Plessur, Gebr. Fretz A.G., Zürich, Switzerland, 128 p., 3 plates.

Nievergelt, P., Liniger, M., Froitzheim, N., & Mählmann, R. F. (1996). Early to mid Tertiary crustal extension in the Central Alps: The Turba mylonite zone (eastern Switzerland). *Tectonics*, *15*, 329–340. https://doi.org/10.1029/93TC02312

Oberli, F., Meier, M., Berger, A., Rosenberg, C. L., & Giere, R. (2004). U-Th-Pb and $^{230}Th/^{238}U$ disequilibrium isotope systematics: Precise accessory mineral chronology and melt evolution tracing in the Alpine Bergell Intrusion. *Geochimica et Cosmochimica Acta*, *68*, 2543–2560. https://doi.org/10.1016/j.gca.2003.10.017

Oldow, J. S., Ferranti, L., Lewis, D. S., Campbell, J. K., D'Argenio, B., Catalano, R., … Aiken, C. L. V. (2002). Active fragmentation of Adria, the North African promontory, central Mediterranean Orogen. *Geology*, *30*, 779–782. https://doi.org/10.1130/0091-7613(2002)030<0779:AFOATN>2.0.CO;2

Oxburgh, E. R., Lambert, R. S. J., Baadsgaard, H., & Simons, J. (1966). Potassium-argon age studies across the southeast margin of the Tauern window, the eastern Alps. *Verhandlungen der Geologischen Bundesanstalt [Wien]*, *1–2*, 17–33.

Peacock, S. M. (1989). Thermal modeling of metamorphic pressure-temperature-time paths: A forward approach. In F. Spear & S. M. Peacock (Eds.), *Metamorphic pressure-temperature-time paths: Short course in geology* (Vol. 7, pp. 57–102). Washington DC: American Geophysical Union.

Peters, T., & Stettler, A. (1987). Radiometric age, thermobarometry and mode of emplacement of the Totalp peridotite in the Eastern Swiss Alps. *Schweizerische Mineralogische und Petrographische Mitteilungen*, *67*, 285–294.

Pfiffner, A. O. (2010). *Geologie der Alpen*, (2. Auflage ed., p. 360). Bern: Haupt UTB.

Philipp, R. (1982). Die Alkaliamphibole der Platta-Decke zwischen Silsersee und Lunghinpass (Graubünden). *Schweizerische Mineralogische und Petrographische Mitteilungen*, *62*, 437–455.

Platt, J. P. (1986). Dynamics of orogenic wedges and the uplift of high-pressure metamorphic rocks. *Geological Society of America Bulletin*, *97*, 1037–1053.

Pleuger, J., & Podladchikov, Y. Y. (2014). A purely structural restoration of the NFP20-East cross section and potential tectonic overpressure in the Adula nappe (central Alps). *Tectonics*, *33*, 656–685. https://doi.org/10.1002/2013TC003409

Price, J. B. (2017). I: Normal faulting on the Austroalpine "overthrust" constrained by thermochronometry and kinematic analysis, Central Alps, Graubünden region, Switzerland. II: Clumped isotope thermometry of carbonate phases associated with the copper deposits of Kennecott, Alaska, unpublished PhD dissertation, California Institute of Technology, 167 p.

Price, J. B., Wernicke, B. P., Cosca, M. A., & Farley, K. A. (2017). Ar/Ar, Zircon Fission Track, Zircon (U-Th)/He, Apatite (U-Th)/He cooling ages from the Austroalpine-Pennine Transition Zone, Eastern Switzerland. *Interdisciplinary Earth Data Alliance (IEDA)*. https://doi.org/10.1594/IEDA/100727

Rahn, M. K. (2005). Apatite fission track ages from the Adula nappe: Late-stage exhumation and relief evolution. *Schweizerische Mineralogische und Petrographische Mitteilungen*, *85*, 233–245.

Ratschbacher, L., Frisch, W., Linzer, H. G., & Merle, O. (1991). Lateral extrusion in the Eastern Alps: Part 2. Structural analysis. *Tectonics*, *10*, 257–271. https://doi.org/10.1029/90TC02623

Reiners, P. W., Brady, R., Farley, K. A., Fryxell, J. E., Wernicke, B. P., & Lux, D. (2000). Helium and argon thermochronometry of the Gold Butte Block, South Virgin Mountains, Nevada. *Earth and Planetary Science Letters*, *178*, 315–326.

Ring, U., Ratschbacher, L., & Frisch, W. (1988). Plate-boundary kinematics in the Alps: Motion in the Arosa suture zone. *Geology*, *16*, 696–698.

Ring, U., Ratschbacher, L., Frisch, W., Biehler, D., & Kralik, M. (1989). Kinematics of the Alpine plate-margin: Structural styles, strain and motion along the Penninic–Austroalpine boundary in the Swiss–Austrian Alps. *Journal of the Geological Society*, *146*, 835–849.

Rubatto, D., & Hermann, J. (2001). Exhumation as fast as subduction? *Geology*, *29*, 3–6.

Rubatto, D., Hermann, J., Berger, A., & Engi, M. (2009). Protracted fluid-induced melting during Barrovian metamorphism in the Central Alps. *Contributions to Mineralogy and Petrology*, *158*, 703–722.

Scharf, A., Handy, M. R., Favaro, S., Schmid, S. M., & Bertrand, A. (2013). Modes of orogen-parallel stretching and extensional exhumation in response to microplate indentation and roll-back subduction (Tauern Window, Eastern Alps). *International Journal of Earth Sciences (Geologische Rundschau)*, *102*, 1627–1654. https://doi.org/10.1007/s00531-013-0894-4

Scheiber, T., Pfiffner, O. A., & Schreurs, G. (2012). Strain accumulation during basal accretion in continental collision: A case study from the Suretta Nappe (Eastern Swiss Alps). *Tectonophysics*, *579*, 56–73. https://doi.org/10.1016/j.tecto.2012.03.009

Schenker, F. L., Schmalholz, S. M., Moulas, E., Pleuger, J., Baumgartner, L. P., Podladchikov, Y., … Müntener, O. (2015). Current challenges for explaining (ultra) high-pressure tectonism in the Pennine domain of the Central and Western Alps. *Journal of Metamorphic Geology*, *33*(8), 869–886. https://doi.org/10.1111/jmg.12143

Schlunegger, F., & Willett, S. (1999). Spatial and temporal variations in exhumation of the central Swiss Alps and implications for exhumation mechanisms. In U. Ring, et al. (Eds.), *Exhumation processes: Normal faulting, ductile flow, and erosion* (Vol. 154, pp. 157–179). Geological Society, London: Special Publications.

Schmid, S. M., & Froitzheim, N. (1993). Oblique slip and block rotation along the Engadine line. *Eclogae Geologicae Helvetiae*, *86*, 569–593.
Schmid, S. M., Fügenschuh, B., Kissling, E., & Schuster, R. (2004). Tectonic map and overall architecture of the Alpine orogen. *Eclogae Geologicae Helvetiae*, *97*, 93–117.
Schmid, S. M., Pfiffner, O. A., Froitzheim, N., Schönborn, G., & Kissling, E. (1996). Geophysical-geological transect and tectonic evolution of the Swiss-Italian Alps. *Tectonics*, *15*, 1036–1064. https://doi.org/10.1029/96TC00433
Schreurs, G. (1993). Structural analysis of the Schams nappes and adjacent tectonic units: Implications for the orogenic evolution of the Penninic Zone in eastern Switzerland. *Bulletin de la Société Géologique de France*, *164*, 415–435.
Schuster, R., & Frank, W. (1999). Metamorphic evolution of the Austroalpine units east of the Tauern Window: Indications for Jurassic strike slip tectonics. *Mitt Ges Geol Bergbaustud Österreich*, *42*, 37–58.
Schuster, R., Scharbert, S., Abart, R., & Frank, W. (2001). Permo-Triassic extension and related HT/LP metamorphism in the Austroalpine–Southalpine realm. *Mitt Ges Geol Bergbaustud Österreich*, *45*, 111–141.
Selverstone, J. (1988). Evidence for east–west crustal extension in the Eastern Alps: Implications for the unroofing history of the Tauern Window. *Tectonics*, *7*, 87–105.
Selverstone, J. (2005). Are the Alps collapsing? *Annual Reviews in Earth and Planetary Science*, *33*, 113–132.
Singleton, J. S., Stockli, D. F., Gans, P. B., & Prior, M. G. (2014). Timing, rate, and magnitude of slip on the Buckskin-Rawhide detachment fault, west central Arizona. *Tectonics*, *33*, 1596–1615. https://doi.org/10.1002/2013TC003517
Steiger, R. H. (1964). Dating of orogenic phases in the central Alps by K-Ar ages of hornblende. *Journal of Geophysical Research*, *69*, 5407–5421.
Steinitz, G., & Jäger, E. (1981). Rb-Sr and K-Ar studies on rocks from the Suretta nappe, eastern Switzerland. *Schweizerische Mineralogische und Petrographische Mitteilungen*, *61*, 121–131.
Steinmann, M. (1994). Ein Beckenmodell für das Nordpenninikum der Ostschweiz. *Jahrbuch der Geologischen Bundesanstalt*, *137*, 675–721.
Stöckli, D. F. (2005). Application of low-temperature thermochronometry to extensional tectonic settings. *Reviews in Mineralogy and Geochemistry*, *58*, 411–448. https://doi.org/10.2138/rmg.2005.58.16
Thöni, M. (1980). Distribution of pre-Alpine and Alpine metamorphism of the southern Ötztal Mass and the Scarl Unit, based on K/Ar age determinations. Mitt. ÖSTERR. GEOL. GES, 71/72, 139–165. Retrieved from http://www.zobodat.at/web4beta/pdf/MittGeolGes_71_72_0139%E2%80%930165.pdf
Trümpy, R. (1960). Paleotectonic evolution of the Central and Western Alps. *Geological Society of America Bulletin*, *71*, 843–907.
Trümpy, R. (1980). *Geology of Switzerland: An outline of the geology of Switzerland: Interbook*.
Vance, D., & O'Nions, R. K. (1992). Prograde and retrograde thermal histories from the Central Swiss Alps. *Earth and Planetary Science Letters*, *114*, 113–129.
Vernon, A. J., Van der Beek, P. A., Sinclair, H. D., & Rahn, M. K. (2008). Increase in late Neogene denudation of the European Alps confirmed by analysis of a fission-track thermochronology database. *Earth and Planetary Science Letters*, *270*, 316–329. https://doi.org/10.1016/j.epsl.2008.03.053
von Blanckenburg, F., & Davies, J. H. (1995). Slab breakoff: A model for syncollisional magmatism and tectonics in the Alps. *Tectonics*, *14*, 120–131.
Wagner, G. A., Reimer, G. M., & Jäger, E. (1977). Cooling ages derived by apatite fission-track, mica Rb-Sr and K-Ar dating: The uplift and cooling history of the Central Alps. In *Memorie degli Instituti di Geologia e Mineralogia dell'Università di Padova* (Vol. 30, pp. 3–25). Società Cooperativa Tipografica.
Weh, M. (1998). Tektonische Entwicklung der penninischen Sediment-Decken in Graubünden (Prättigau bis Oberhalbstein). Unpublished PhD thesis, University of Basel, 230 p.
Weh, M., & Froitzheim, N. (2001). Penninic cover nappes in the Prättigau half-window (eastern Switzerland): Structure and tectonic evolution. *Eclogae Geologicae Helvetiae*, *94*, 237–252.
Wheeler, J., Reddy, S. M., & Cliff, R. A. (2001). Kinematic linkage between internal zone extension and shortening in more external units in the NW Alps. *Journal of the Geological Society of London*, *158*(3), 439–443.
Wiederkehr, M., Bousquet, R., Schmid, S. M., & Berger, A. (2008). From subduction to collision: Thermal overprint of HP/LT meta-sediments in the north-eastern Lepontine Dome (Swiss Alps) and consequences regarding the tectono-metamorphic evolution of the Alpine orogenic wedge. *Swiss Journal of Geosciences*, *101*, 127–155.
Wiederkehr, M., Sudo, M., Bousquet, R., Berger, A., & Schmid, S. M. (2009). Alpine orogenic evolution from subduction to collisional thermal overprint: The $^{40}Ar/^{39}Ar$ age constraints from the Valaisan Ocean, central Alps. *Tectonics*, *28*, TC6009. https://doi.org/10.1029/2009TC002496
Wiederkehr, M., Bousquet, R., Ziemann, M. A., Berger, A., & Schmid, S. M. (2011). 3-D assessment of peak-metamorphic conditions by Raman spectroscopy of carbonaceous material: an example from the margin of the Lepontine dome (Swiss Central Alps). *International Journal of Earth Sciences*, *100*(5), 1029–1063.
Wust, G. H., & Silverberg, D. S. (1989). Northern Combin zone complex-Dent Blanche nappe contact: Extension within the convergent Alpine Belt. *Schweizerische Mineralogische und Petrographische Mitteilungen*, *69*, 251–259.
Wyss, R., & Isler, A. (2011). *1214 Ilanz Erläuterungen, Geologischer Atlas der Schweiz*. Swisstopo: Bundesamt für Landestopografie.
York, D., Evensen, N. M., Martı´nez, M. L., & De Basabe Delgado, J. (2004). Unified equations for the slope, intercept, and standard errors of the best straight line. *American Journal of Physics*, *72*, 367–375.
Ziegler, W. H. (1956). Geologische studien in den flyschgebieten des Oberhalbsteins (Graubünden). *Eclogae Geologicae Helvetiae*, *49*, 1–81.